DESIGN AND DEVELOPMENT OF MACH-ZEHNDER INTERFEROMETER FIBER SENSOR FOR STRUCTURAL HEALTH MONITORING

By

PNG WEN HAO

A dissertation submitted to the Department of Electrical and Electronics Engineering,
Lee Kong Chian Faculty of Engineering & Science,
Universiti Tunku Abdul Rahman,
in partial fulfillment of the requirements for the degree of
Master of Engineering Science
Jan 2019

ABSTRACT

DESIGN AND DEVELOPMENT OF MACH-ZEHNDER INTERFEROMETER FIBER SENSOR FOR STRUCTURAL HEALTH MONITORING

Png Wen Hao

Structural health monitoring is important to our life as losses in resources and lives can occur if deflection and damage of civil structure and pipeline system can not be detected immediately. This thesis presents a novel study on structural health monitoring based on optical fiber sensor, which includes the curvature sensing and crack monitoring using the packaged fiber-based in-line tapers Mach-Zehnder Interferometer (MZI) curvature sensor, as well as the Loop integrated Mach-Zehnder Interferometer (LMZI) optical fiber sensor in pipeline monitoring and vibration sensing.

A highly sensitive tapers MZI sensor with curvature sensitivity up to 1.65 $\mu W/m^{-1}$ was fabricated and implemented in concrete monitoring. In the lab tests, three MZI sensors were embedded into the Lightweight Foamed Concrete Structural (LWFCS) beams with different polypropylene percentages (0.4 %, 0.25 % and 0 %) to characterize the sensor performance according to the concrete environments of different tensile capacities. MZI sensor managed to hold up to a maximum loading force of 26 kN in the concrete environment before it stopped functioning. The resultant optical powers of MZI sensors were mapped to the strains measured by the lead wire alloy foil strain gauges (brand:

TML, model: FLK-6-11), and achieved a good correlation up to 0.968. Furthermore, double-sided sensing property of MZI sensor had advantage over the conventional strain gauge in detecting the internal cracking of concrete before any earlier sighting of the surface macrocracks.

A low frequency vibrational LMZI sensor with torsional sensitivity up to 0.0216 μW/° was fabricated and implemented in the pipeline monitoring. The LMZI sensor was characterized according to the discrete changes of frequencies range from 20 Hz to 500 Hz and showed good accuracy and reliability in the frequency response. In both 3 m galvanized steel pipeline and 40 m large scale pipeline test, the LMZI sensor able to detect the vibrations induced by the water flow during normal flow conditions, as well as the additional leak-induced vibrations during the leak events. The frequency responses of the LMZI sensor were compared to the Accelerometer (model: Kistler 8704B50T) and show good agreement with percentage variations of 0.4% and 2.64% in the 2 bar and 3 bar, respectively.

ACKNOWLEDGEMENTS

My highest gratitude to my supervisor, Prof Faidz Abd Rahman and my co-supervisor, Dr Lin Horng Sheng. They have given plenty of constructive suggestions and clear guidance while I was completing my research. A good ethic of research was inculcated by them during the period of my master's degree.

This material is based upon work performed at University Tunku Abdul Rahman for Center of Photonics and Advance Materials as well as supported by Grant TRGS/1/2016/UTAR/01/2/1 and UTARRF/2017-C1/L15.

APPROVAL SHEET

This dissertation/thesis entitled "**DESIGN AND DEVELOPMENT OF MACH-ZEHNDER INTERFEROMETER FIBER SENSOR FOR STRUCTURAL HEALTH MONITORING"** was prepared by PNG WEN HAO and submitted as partial fulfillment of the requirements for the degree of Master of Engineering Science at Universiti Tunku Abdul Rahman.

Approved by:

_____

(Faidz Abdul Rahman) Date:……..
Professor/Supervisor
Department of Electrical and Electronics Engineering
Lee Kong Chian Faculty of Engineering & Science
Universiti Tunku Abdul Rahman

_____

(Lin Horng Sheng) Date:……..
Professor/Co-supervisor
Department of Electrical and Electronics Engineering
Lee Kong Chian Faculty of Engineering & Science
Universiti Tunku Abdul Rahman

LEE KONG CHIAN FACULTY OF ENGINEERING AND SCIENCE

UNIVERSITI TUNKU ABDUL RAHMAN

Date: _____

SUBMISSION OF FINAL YEAR PROJECT /DISSERTATION/THESIS

It is hereby certified that ***Png Wen Hao*** (ID No: ***1701263***) has completed this final year project/ dissertation/ thesis* entitled "*Design and Development of Mach-Zehnder Interferometer Fiber Sensor for Structural Health Monitoring*" under the supervision of Prof. Faidz Abd Rahman (Supervisor) from the Department of Electrical and Electronic Engineering, Lee Kong Chian Faculty of Engineering and Science , and Dr. Lin Horng Sheng (Co-Supervisor)* from the Department of Electrical and Electronic Engineering, Lee Kong Chian Faculty of Engineering and Science.

I understand that University will upload softcopy of my final year project / dissertation/ thesis* in pdf format into UTAR Institutional Repository, which may be made accessible to UTAR community and public.

Yours truly,

_____

(*Png Wen Hao*)

*Delete whichever not applicable

DECLARATION

I hereby declare that the dissertation is based on my original work except for quotations and citations which have been duly acknowledged. I also declare that it has not been previously or concurrently submitted for any other degree at UTAR or other institutions.

Name _____

Date _____

LIST OF TABLES

LIST OF FIGURES

LIST OF ABVREVIATIONS

FBG	Fiber Bragg grating
FSR	Free spectral range
LMZI	Loop-integrated Mach-Zenhder Interferometer
LPG	Long period grating
LVDT	Linear variable displacement transducer
LWFCS	Lowweighted foamed concrete structural
MI	Michelson Interferometer
MZI	Mach-Zehneder Interferometer
NDT	Non-destructive test
OLTS	Optical loss test sets
OSA	Optical spectrum analyzer
PCF	Photonics crystal fiber
SHM	Structural health monitoring
SMM	Subcarrier Multiplexing Method
TDM	Time Division Multiplexing

TABLE OF CONTENTS

CHAPTER 1

INTRODUCTION

1.1 Structure Health Monitoring

Structural Health Monitoring (SHM) is commonly implemented in structural inspection of the large scale civil structures such as bridges, buildings, dams, vessels and platforms. In 2016, 7 severe building failures were reported in Malaysia which resulted in 15 injuries and 4 deaths. The possible factors causing the building failures were reported as the strength of the foundation, supporting strength of the concrete structure, improper curing process and lack of inspection (Dermawan, 2016; Achariam, 2016; Mohd, 2016; Koh, 2015; Mohd, 2016). Consequently, the government and private industries are growing concern over the SHM in term of the structural inspections and safety maintenances.

There are various types of prevalent inspection methods using the traditional vibration sensors, such as the magneto-electric, piezoelectric, line scanning thermography and current sensor. In most of the non-destructive tests (NDTs), electromagnetic waves are generated and projected into the structure, reflections happen as the waves meet the discontinuities. From the reflected signals, condition of the structural health such as damage and crack can be localized. However, the damping property of most materials cause attenuation in the reflected waves which in turn lead to an underrating and inaccurate estimation of the severe damage (Yang & Hu, 2008).

According to the National Water Services Commission (SPAN, the non-revenue water (NRW) accounted for 35.2% water loss in 2016, which is about 5.47 billion litres per day and equivalent to the 4 days continuous water supply to our capital, Kuala Lumpur (National Water Services Commission, 2017). Leakages in the fluid transportation cause tremendous loss to utility suppliers and gas industries which are essential to our life, thereby arose the awareness of SHM in the vessels and pipelines. Several NDTs have grown popular in the vessel inspection such as the acoustic emission, electromagnetic acoustic transducer, and the Computed Tomography (CT) scanner.

1.2 Problem Statement

The destructions and losses brought by the failure in concrete and pipeline rupture are heavily impact our daily life, the structural health monitoring is now acutely aware. Recently, the applications of optical fiber sensors are prevailing among the NDTs as the physical properties of the optical fiber sensors preponderate the conventional electronics sensors in many ways. Firstly, the optical fiber sensors are nonconductive and immune to electromagnetic interference, which have advantage over the conventional electronics sensor under conductive environments. Besides, the optical fiber sensors are made of silica which have good resistance to corrosion and invisible to the intruders, therefore suitable to be implemented at the outdoor sensing environments. However, optical fiber sensors those rely on refractive index modulation such as the fiber Bragg grating (FBGs) and long period grating (LPG) sensor required a complicated and high-cost fabrications. In addition, the instrumental supports are always the downside of the grating based optical fiber

sensors when involving the optical interrogator and optical spectrum analyzer which are inconvenient to be carried and installed at the test sites.

1.3 Aims and Objectives

A few objectives of the project are stated as follow to solve the aforementioned issues in the problem statement:

1. To design and fabricate an optical sensor which is cost-effective, relatively simple in fabrication and able to cater for both concrete and pipeline monitoring.
2. To characterize the sensing parameters and sensitivities of the optical fiber sensor in term of each field of monitoring (curvature in concrete monitoring and vibration frequency in pipeline monitoring).
3. To implement the optical fiber sensor in the lab tests (LWFCS beam for concrete monitoring and 40 m galvanized pipeline for pipeline monitoring) and compare the capability with the convention sensors.

1.4 Thesis Outline

This thesis comprises of five chapters where the details of each chapters are described as follows:

- Chapter 1 gives a brief introduction on SHM, types of conventional sensors and sensing methods, problem statement as well as the objectives of the project.

- Chapter 2 reviews curvature sensing in concrete beams and vibration sensing in pipeline, as well as various types of interferometer sensors and their fabrication methods. Besides, detailed discussion on the sensing principle of the MZI sensor and the LMZI sensor were included in the literature review.
- Chapter 3 focuses on the methodology of this project, which includes the fabrications, packagings, characterizations and lab tests of the sensors in concrete and pipeline monitoring.
- Chapter 4 comprises the analyses and discussions of the results in the characterizations as well as lab tests of both MZI sensor and LMZI sensor in terms of curvature and vibration sensing, respectively.
- Chapter 5 concludes all the completed works and discusses some recommendations for the future works.

CHAPTER 2

LITERATURE REVIEW

2.1 Concrete monitoring

Curvature sensing and crack inspection are equally important in concrete monitoring to ensure the structural health of the civil structure. Curvature sensing monitors the internal condition of the reinforcement bars such as the elongation and bending. Crack inspection ensure the internal health of the beam structure by tracking any possible defections and fractures within the concrete.

Deformation of the reinforced concrete (RC) beam usually involves two types of deformations: the elastic deformation and inelastic deformation, which resulted from different materials' properties such as ductility and Young's modulus (stress-strain relationship) of the concrete and reinforcement bar (rebar). Different elongations or strain behaviors of the concrete and rebar cause non-consistent internal and external curvatures along the RC beam. Owing to inelastic property of concrete, crack is expected occurs immediately as the elongation exceeded the rebar's tensile capacity (Meyers & Chawla, 2008). Therefore, several groups of researchers have implemented the acoustic emission (AE) sensing method in crack monitoring, to detect the instantaneous pulse generated by the concrete during the crack initialization (Aggelis, et al., 2011; Li, et al., 2016; Shiotani, et al., 2010).

Moreover, other groups of researchers conducted the curvature inspection by observing the curvature changes of the rebar inside the RC beam using the conventional strain gauge (Charif & Mourad, 2016; Kwak & Kim, 2002; Taghreed, 2014). The curvature is expected to increase as the load is consistently imposed to the RC beam. The flexural behaviors of rebar vary with the degree of loading, which consist of two phases, the elastic elongation and yielding.

2.2 Pipeline monitoring

Water flow in pipeline causes vibration on the pipe surface due to the impact of water onto the inner wall of pipe. In general, leak creates sound when the water escapes from the leak hole because of the turbulent jet generated during leak interacts with the pipe wall, thereby incurs the turbulent pressure fluctuation (Khulief & Khalifa, 2012; Hunaidi, et al., 2004).

The sound-generation mechanism of leak is different at low and high frequencies. Unsteady flow separation at the leak site results in low frequency signal, whereas high frequency signal is triggered during cavitation (Thompson, et al., 2001). When the velocity of escaping water from the leak hole is high enough to cause a drop in the inner water pressure, the vapor bubbles are expected to form as the water pressure drops below the vapor pressure of the liquid. The imploding bubbles impact on the pipe wall, and thus create sound with different frequencies due to different sound-generation mechanisms (Khulief & Khalifa, 2012).

The traditional acoustic leak-detection methods such as the listening rod, aqua phone, and ground microphone are straightforward but the non-consistent in the effectiveness as these methods usually depend on the experience of the user. Later, the acoustic techniques are prevalently implemented in the leak detection in the water-distribution systems (Hunaidi, 1998). Accelerometer or microphone were used as the surface-mounted sensors, to measure the leak-induced vibration on the pipe wall. These devices are typically attached to the fire hydrants, valves or other contact points of the pipe (Hunaidi, et al., 2004). The spectrum of the acoustic emission signal induced by leak is significantly different compared to the background signal even when the measurement was taken under low pressure water flow (Raijtar, et al., 1994).

Hydrophone is another type of sensor caters for the in-pipe measurement. It is usually inserted into the inner column of pipeline through opening on hydrant or other outlet and travel with the flow inside the pipe. Hydrophone required to be in contact with the water column in order to detect the acoustic noise transmitted through the water column. The direct acoustic measurements through hydrophones preponderate other sensors those rely on the surface transmission of vibration. However, the major drawback of hydrophones is the perturbation of velocity and pressure inside the pipe due to the turbulent at the bends and elbows of pipeline which may interfere with the leak generated wave (Barabanov & Glikman, 2009).

Low frequency sensing is preferred in the long-distance pipeline monitoring as low frequency waves are capable to travel through long distance along pipeline without excessive damping (Rocha, 1989). Moreover, most of the researchers reported that the leak event induces low frequency vibrations,

which range from the lowest 1.5 Hz up to few hundred Hertz (Aimé, et al., 2009; Karkulali & Mishra, 2016).

2.3 Interferometric Optical Fiber Sensor

Interferometric optical fiber sensor is one of the prevalent optical sensor which has a relative simple optical and instrumental set-up compared to other optical fiber sensor such as FBGs and LPGs, which is much convenient to be implemented at the test site. In general, there are three types of interferometric sensors which are prevalent in different sensing applications, those are the Fabry-Perot, Mach-Zehnder and Michelson, interferometer sensor.

2.3.1 Fabry-Perot Interferometer Sensor

A Fabry-Perot interferometer (FPI) consists of two parallel reflecting surfaces which are separated by a certain distance, to reflect and transmit the input light and create a multiple superpositions signal at the output (Pedrotti, et al., 2007; Sirkis, et al., 1973). The FPI sensor can be classified into the intrinsic and extrinsic FPI sensor (Tsai & Lin, 2001). Figure 2.1 (a) shows the structure of the intrinsic FPI sensor whereby the optical fiber is integrated with two reflecting components with separation distance. Figure 2.1 (b) depicts the extrinsic FPI whereby the optical fiber segment is separated by an air column. The intrinsic FPI can be fabricated using various of fabrication technique, such as micro machining (Ran, et al., 2009; Ran, et al., 2008; Rao, et al., 2007), fiber Bragg gratings (FBGs) (Wan & Taylor, 2002; Wang, et al., 2007), chemical etching (Zhang, et al., 2007; Machavaram, et al., 2007), and thin film deposition

(Zhao, et al., 2010; Morris, et al., 2009). The extrinsic FPI sensor can be fabricated using the elaborate laser machining process (Ran, et al., 2009; Rao, et al., 2007). Both of the reflecting components of the intrinsic FPI and air cavity of extrinsic FPI cause the optical path length difference (OPD) between the reflected and transmitted lights, whereby the optical phases difference changes accordingly with the external perturbation.

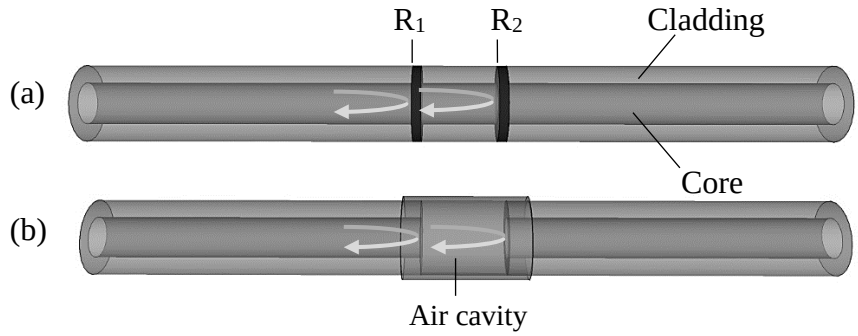

Figure 2.1: (a) Intrinsic FPI sensor formed by two reflecting components, R1 and R2, along a fiber, and (b) extrinsic FPI sensor made by forming an external air cavity.

The extrinsic FPI sensors were commonly implemented in the refractive index (RI) sensing because the air column within the extrinsic cavity can be easily filled by another solution (Mudhana, et al., 2011; Mudhana, et al., 2011; Choi, et al., 2008). Moreover, strain sensings using the intrinsic FPI sensors were reported by few groups of researchers, whereby the micro-structured optical fibers (MOFs) or FBGs act as the intrinsic cavities of sensors (Frazao, et al., 2009; Deng, et al., 2011; Chen, et al., 2009). However, these types of intrinsic FPI sensors are complicated to be fabricated when involving the MOFs and FBGs.

2.3.2 Mach-Zehnder Interferometer Sensor

Another commonly found Interferometric sensor is the Mach-Zehnder interferometer (MZI). By implementing the modal dispersion, the MZI splits the light beam into two paths, one acts as the reference to another, namely the reference arm and the sensing arm. As shown in Figure 2.2, the optical fiber is split into two paths by a 3dB coupler and recombined at the output. The sensing arm is exposed to the external perturbation while the reference arm is kept in the undisturbed condition. MZIs sensing principles are widely used in sensing field such as strain sensing (Liu & Wei, 2007; Choi, et al., 2007), curvature sensing (Shen, et al., 2012; Gong, et al., 2011; Dass & Jha, 2015), temperature sensing (Lu & Chen, 2010; Chen, et al., 2014), refractive index sensing (Tian, et al., 2008; Gao, et al., 2013), and vibration sensing (Shun, et al., 2014; Ben, et al., 2012).

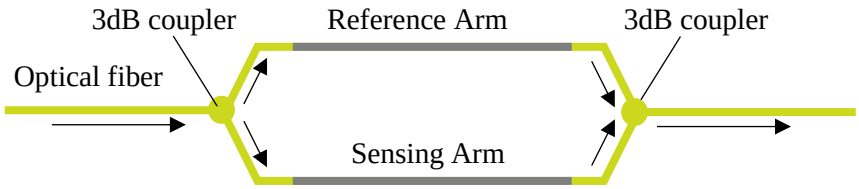

Figure 2.2: The schematic diagram of sensing and reference arm of MZI.

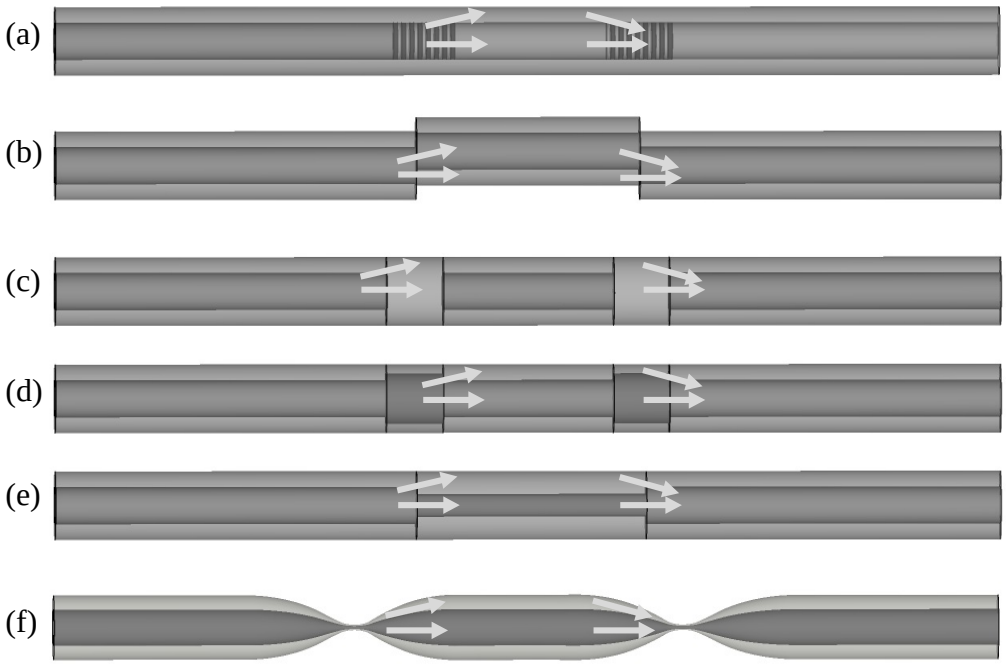

Figure 2.3: Various types of in-line MZI (a) a pair of LPGs, (b) core mismatch, (c) air-hole collapsing of PCF, (d) MMF segment, (e) small core SMF, and (f) fiber tapering.

By manipulating the fiber structure, the modal dispersion using separated arms can be replaced by few types of in-line MZIs. Figure 2.3 depicts several types of in-line MZIs, including the pair long period fiber gratings (LPGs) (Lim, et al., 2004; Kim, et al., 2002; Allsop, et al., 2002; Kim, et al., 2008; Ding, et al., 2005), core mismatch (Kim, et al., 2008; Ngyuen, et al., 2008), air-hole collapsing of photonic crystal fibers (PCFs) (Choi, et al., 2007; Choi, et al., 2008), multiple mode fiber (MMF) segment (Zhu, et al., 2010; Frazao, et al., 2010), small core SMF (Tian, et al., 2008), and fiber tapering (Lin, et al., 2016; Lu, et al., 2009; Mokhtar, et al., 2011). Table 2.1 summarizes the fabrication methods of all the sensors mentioned above, as well as compares the complexities and costs of each fabrications.

Table 2.1: Summarization table of the in-line interferometer scheme.

In-line MZI	Fabrication method	Fabrication complexity	Fabrication cost	Drawbacks
LPGs	• Periodic modulation in the RI of the fiber core by UV light (Kim, et al., 2008) • CO_2 laser (Kim, et al., 2002; Allsop, et al., 2002) • Mechanical press by periodic pressure along PCF (Lim, et al., 2004)	High	High	• Works only in a limited band(s) of wavelengths due to phase matching phenomenon of fiber gratings
Core mismatch	• Splicing two fibers with a minute lateral offset (Choi, et al., 2007)	Low	Low	• Mechanically weak especially at the splicing region
Air-hole collapsing of PCF	• Splicing of the PCF-LPG PCF and electric arc discharge to collapse the PCF into air hole (Choi, et al., 2008)	High	High	• Difficulty in controlling and coupling the cladding modes • Insertion loss is high
Small core SMF	• Splicing of the SMF and the Thin-Core Fiber (TCF)	Low	High	• Not applicable
Fiber taper	• Laser ablation (Morales & Lieber, 1998) • Fiber pulling (Clohessy, et al., 2005) • Direct draw from bulk materials (Xing, et al., 2008) • Concatenating Two SMF Tapers using fusion splicer (Tian, et al., 2008)	Low	Low	• mechanically weak especially at the taper region

2.3.3 Michelson Interferometer Sensors

Similar to the MZI, Michelson Interferometer (MI) sensor splits the beam into two light paths by modal dispersion. Beams at different modes are split into two optical paths and reflected at each end. Figure 2.4 illustrates the schematic diagram of the modal splitting in the MI interferometer, whereby the sensing principle involves the sensing arm and reference arm is similar to the MZI. Figure 2.5 indicates the MI structure of a LPG-based compact in-line MI where LPG functions to split the beam into the cladding from the fiber core. Both of cladding and core modes are being reflected at the ends of fiber by two pieces of reflectors.

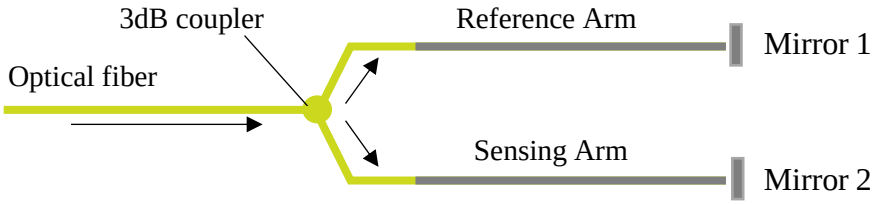

Figure 2.4: The schematic diagram of sensing and reference arm of MI interferometer.

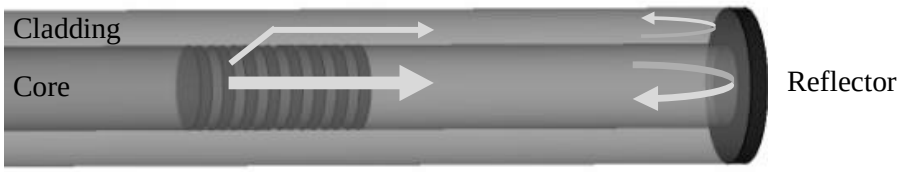

Figure 2.5: The Schematic diagram of a compact in-line MI interferometer

The LPG-based MI sensor is widely used in RI and temperature sensing (Kim, et al., 2005; Brakel & Swart, 2005; Park, et al., 2010; Yuan, et al., 2008). Similar to the extrinsic FPI sensors, the LPG-based MI is easily implemented in the RI measurement by immersing the sensor into the liquid specimen. However, Park, et al. reported that the temperature sensitivity of MI sensor is

much lower in the PCF-based MI sensor (Park, et al., 2010), which is a good measure to reduce or eliminate the temperature dependency in the RI measurement. Nevertheless, the fabrication techniques of both the LPG and PCF-based MI sensors are complicated. Besides, the PCF-based MI sensor has a high fabrication cost when involving the PCF.

In overall, both the core mismatch MZI and fiber tapers MZI have low fabrication complexity and cost among all other interferometer sensors. However, the mechanical strength of the of taper MZI is higher compared to the core mismatch MZI. Besides, the structure of fiber taper is easily fit into the sensor packaging compared to the step-up mismatch core MZI. More importantly, the sensitivity of the tapers MZI can be easily controlled by manipulating the taper diameter (Yang, et al., 2011; Shiotani, et al., 2010; Liu, et al., 2015; Liao, et al., 2013) and the interferometric length (Mao, et al., 2015), which is flexible and customizable in term of structure design to cater for various applications.

2.4 Sensing Principle of Taper-based MZI Sensor

The in-line tapers MZI sensor consists of two tapers whereby mode splitting occurs at the first taper and mode coupling at the second. Figure 2.6 illustrates a bi-conic necking structure of the fiber taper. The narrowing of fiber core diameter causes shrinkage in the *V*-number, which in turn contributes to mode splitting at first taper. Equation (1) shows the relationship between the *V*-number and the narrowing in fiber core radius, *a* (Yin, et al., 2008). Where *V* is the *V*-number, *a* is the fiber core radius, λ is the wavelength of input signal, n_{co} is the refractive index of core, n_{cl} is the refractive index of cladding.

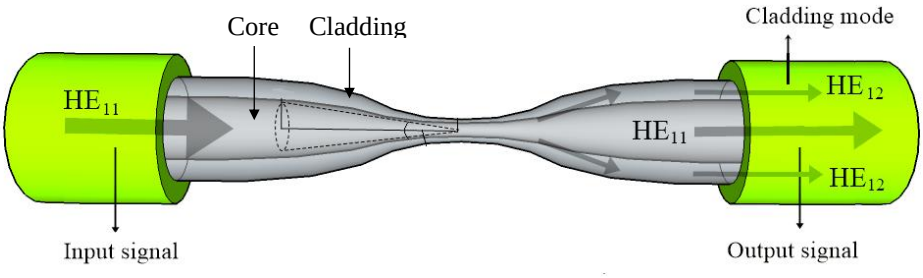

Figure 2.6: The schematic diagram of a fiber taper.

$$V = \frac{2\pi}{\lambda} a \sqrt{n_{co}^2 - n_{cl}^2} \tag{1}$$

Figure 2.7 indicates the complete mode splitting and recoupling process in the MZI sensor, which consists of (a) the mode splitting of the fundamental mode to the cladding mode at the first taper, (b) propagation of the cladding mode within the cladding along the interferometric length, and (c) the recoupling the cladding mode back into the fundamental mode at the second taper. Owing to the intrinsic leak property of the cladding, the cladding mode is weakly guided along the interferometric length and therefore survives shortly within the path.

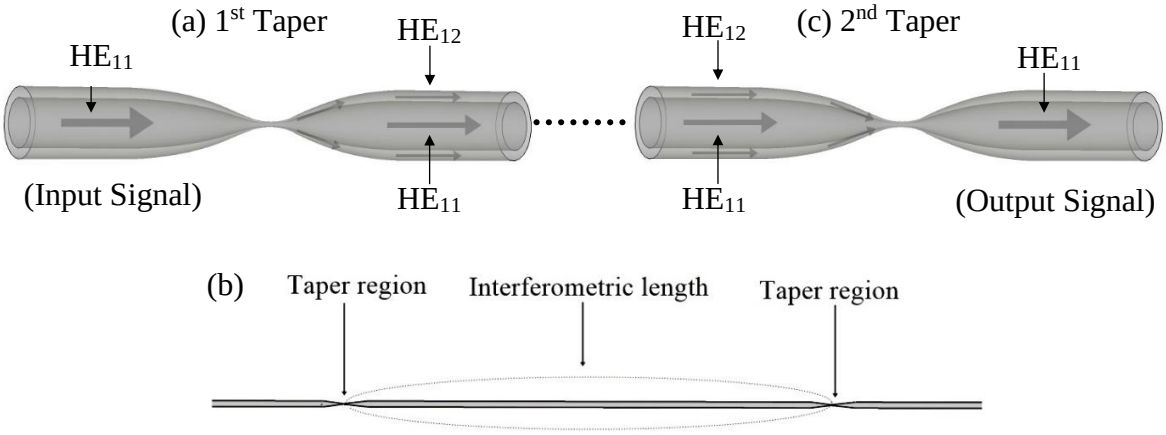

Figure 2.7. The schematic diagram (a) the mode splitting at the first taper, (b) propagation of the cladding mode within the cladding layer along the interferometric length, and (c) the recoupling at the second taper region.

The mode recoupling at the second taper results a modal interference at the output signal. The total intensity, $I(\lambda)$ of output signal is defined by the interference equation as equated in Equation (2) (Yin, et al., 2008). Where $I_1(\lambda)$ and $I_2(\lambda)$ is the intensity of the fundamental mode (HE_{11}) and cladding mode (HE_{12}) at wavelength λ, n_{eff} is the effective refractive index difference of the core and cladding, L is the interferometric length. Moreover, the free spectral range (FSR) of the MZI is equated in Equation (3).

$$I(\lambda) = I_1(\lambda) + I_2(\lambda) + 2\sqrt{I_1(\lambda)I_2(\lambda)}\cos\left[\frac{2\pi\Delta n_{eff}L}{\lambda}\right] \quad (2)$$

$$FSR \approx \frac{\lambda^2}{\Delta n_{eff}L} \quad (3)$$

By referring to Equations (2) and (3), the power intensity and FSR are commonly affected by the interferometric length, L, which made the interferometric length a strain sensing component in the MZI. The changing in interferometric length incurs combinative variations of the output signal in terms of the power intensity and shifting in the FSR. Figure 2.8 shows the of the power fluctuation and shift in FSR when the interferometric length of MZI is elongated from 20 cm to 40 cm.

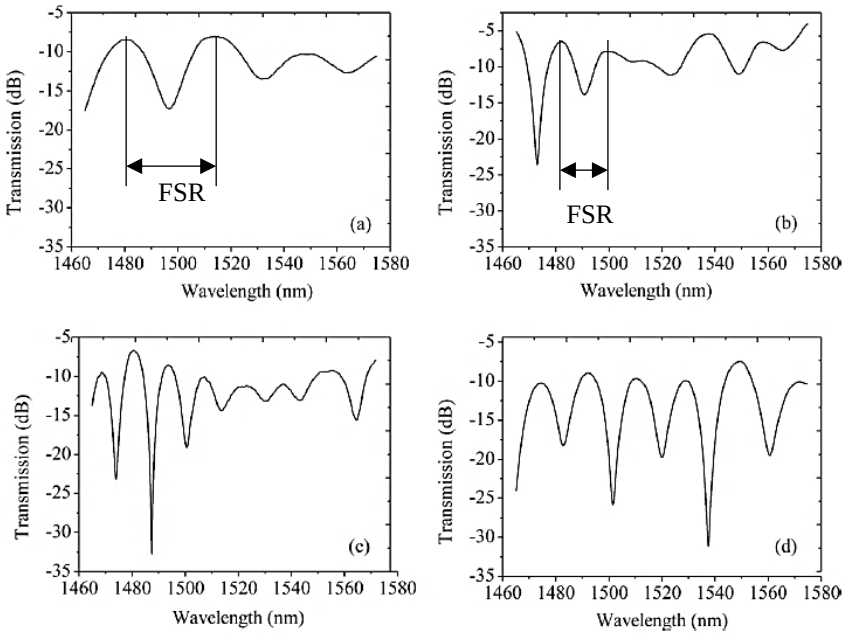

Figure 2.8: The output spectra of MZI under different interferometer lengths: (a) 20 mm, (b) 30 mm, (c) 36 mm and (d) 40 mm (Li, et al., 2011)

2.5 Sensing Principle of LMZI Sensor

The LMZI sensor is proposed to resolve the low vibrational sensitivity issue of the in-line tapers MZI sensor. A fiber loop segment is integrated into the conventional in-line tapers MZI as an amplifying element, whereby the vibration from external source can be coupled effectively into the sensor by mean of torsion effect. The LMZI sensor consists of two sensing elements, where the fiber loop functions as the vibration coupling element, and the tapers functions as the power demodulation element. Vibration is coupled to the fiber loop and exerts periodic torsion to the tapers, whereby varies the power intensity at the output. Power demodulation is relative simple in the torsion-sensitive taper, as the optical power changes linearly with the torsional angle (Zhou, et al., 2015; Chen, et al., 2014; Ni, et al., 2017)

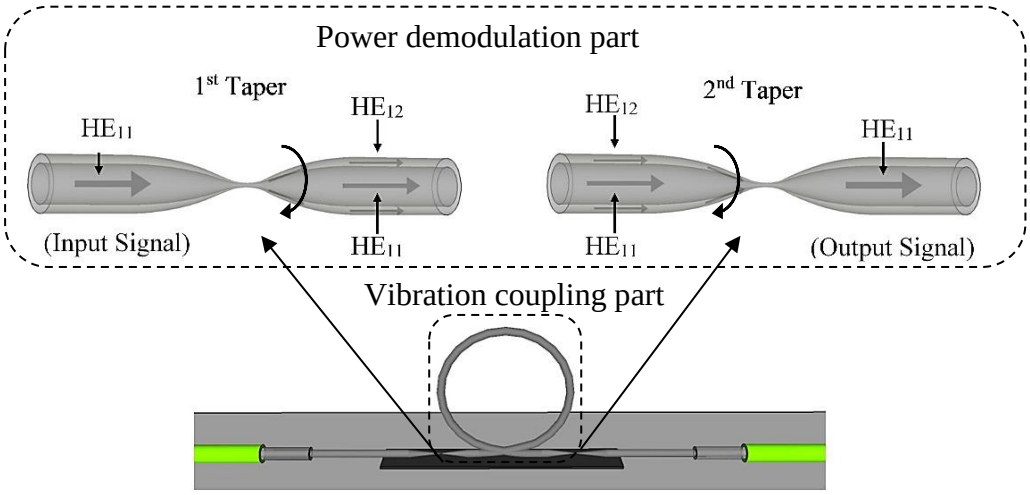

Figure 2.9: The schematic diagram of the vibration coupling and power demodulation parts of the LMZI sensor

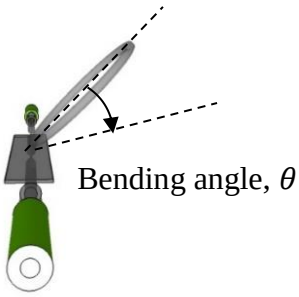

Figure 2.10: Torsion of LMZI sensor

This kind of modification incurs an amplifying effect in the power attenuation of MZI, thereby increases the vibrational sensitivity of sensor. Study done by Harris and Castle found that the bending loss of the single mode fiber has an exponential relation with the length of fiber bend *L* (Harris & Castle, 1986). As shown in Equation (4), the output power decreases exponentially with the length of fiber bend. Where P_o is the output power, P_i is the input power, α is the bending loss coefficient, and *L* is the circumference length of the bending.

$$P_o = P_i e^{-2\alpha L} \tag{4}$$

It is worth to be noted that the radius of the fiber loop will highly attenuated the power in MZI, the sensitivity may degrade if the fiber loop is too small. The fact that a smaller bend radius is contributing to a higher bending loss was studied by Ong et al. by comparing the bending loss of SMF-28 fiber with bend radii range from 5 to 14 mm at wavelength 1550 nm. Besides, a critical radius of 8 mm was reported which is the radius of fiber loop when the bending loss is equal to the 3dB loss. The fiber loop with 7.5 mm was reported managed to respond to the vibration clear and accurately (Ong, et al., 2017).

2.6 Limitations of the MZI Sensors

Cross sensitivity is a common issue in the tapers MZI sensor as the MZI is sensitive to various of perturbations such as temperature, pressures and strain. Temperature is the major disturbance during all other measurements, Raji, et al, have reported a feasible temperature compensation method by using the transfer function matrix, by pre-characterized temperature and strain coefficient (Raji, et al., 2016). Another group of researchers proposed a compensation method in physical way by using the external coating material (Jong, et al., 2016). Simultaneous measurement done by Raji, et al. reported that the uncoated SMF tapers MZI has a curvature and thermal sensitivities of 12.4885dBm/m^{-1} 0.0833dBm/°C, whereby the temperature dependency of the MZI is insignificant.

The limitation of the MZI sensor in concrete monitoring is non-adaptiveness to the existing building, as the implementation requires embedment of sensor in the concrete beam. Therefore the MZI sensor is suggested to be implemented during the building process of civil structure. The

issue is inevitable as the sensor needs to be attached on the reinforcement bar and embedded within the concrete beam in order to measure the curvature of rebar and internal crack.

Besides, MZI sensor is less significantly sensitive to the vibration. Therefore in pipeline monitoring, the pristine MZI sensor was modified slightly in term of the structure to improve the sensitivity.

CHAPTER 3

METHODOLOGY

This project comprises two focuses of SHM: the concrete monitoring and pipeline monitoring by using MZI sensor and LMZI sensor, respectively. The outline of the methodology is plotted in Figure 3.1 which comprises of the fabrications, packagings, characterizations and filed tests of the MZI and LMZI sensors. Fabrication of sensors focus on the optical design criteria such as the taper diameter, interferometer length and radius of fiber loop. Whereas the packagings are proposed to strengthen of the optical structures and enhance the adaptivity of the optical sensors in different sensing environments. The MZI and LMZI sensors are characterized in terms of curvature and frequency, respectively before the lab tests. To simulate the practical condition of real sensing environment, in the lab tests, the MZI sensor will be embedded into three LWFCS beams for strain sensing, whereas the LMZI sensor will be deployed onto a lab-scale pipeline and a 40 m large-scale pipeline for leak detections.

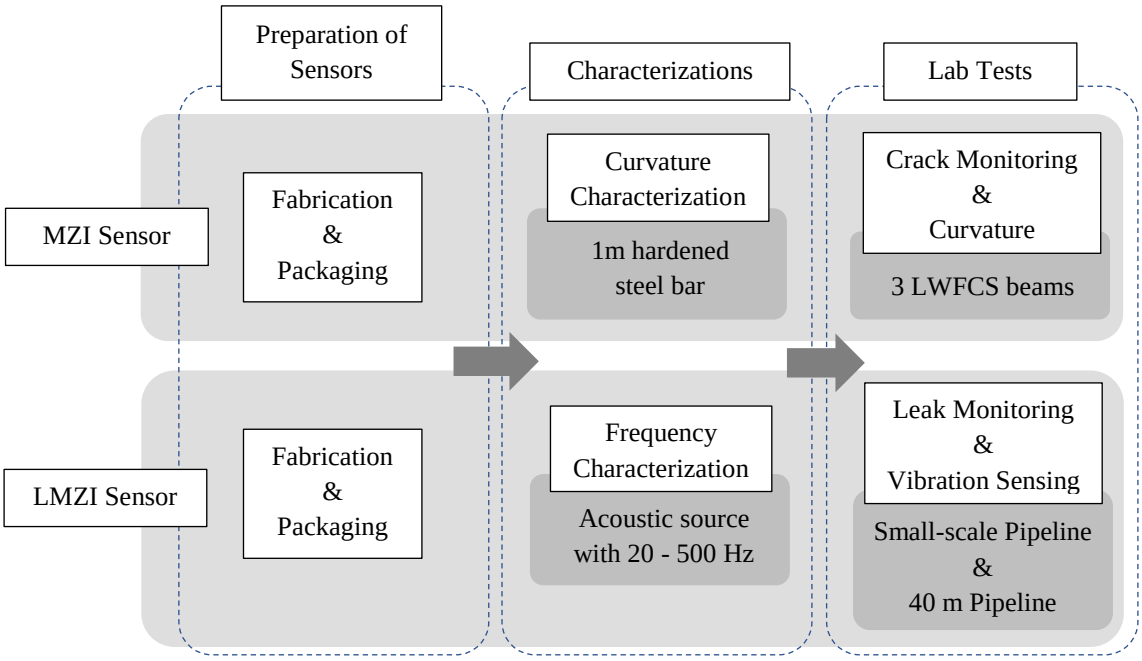

Figure 3.1: Outline of Methodology.

3.1 Fabrication of MZI Sensor

An in-line tapered MZI sensor was fabricated by using an in-house built arc discharge pulling rig (as shown in Figure 5), to create two abrupt bi-conic tapers on a single mode fiber. In order to meet the threshold for mode splitting, both of the bi-conic tapers were controlled down to a minimum acceptance diameter of 0.05 mm (Wang, 2012). Figure 3.2 shows the image of the first and second tapers captured using the digital microscope, both of the tapers were fabricated down to 0.025 mm. It is equally important that a short interferometric length in fact contributes to a wider Free Spectral Range (FSR) profile (Wang, 2012), which in turn achieves a larger linear operating region in the output spectrum. A minimum interferometric length of 2 cm was achieved in this research, with 30 nm FSR as calculated using Equation (3), which is expected to have a sufficiently large linear functionality region.

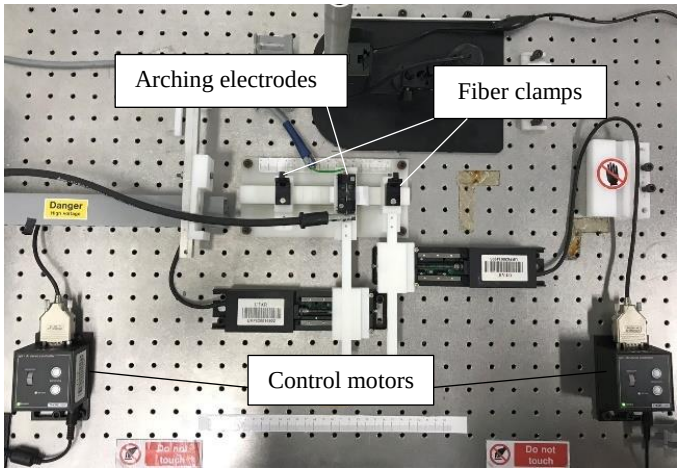

Figure 3.2: The captured image of the in-house fabricating rig.

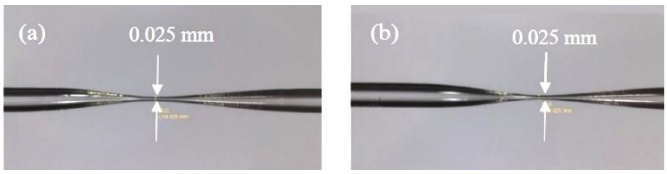

Figure 3.3. The captured image of (a) first (b) and second abrupt biconic tapers of in-line MZI Sensor.

3.2 Packaging of MZI Sensor

The packaging design was introduced into the MZI sensor for purpose of protection under harsh condition of the real sensing environment. Besides, a cover-all packaging in the MZI sensor also eliminates the influences such as humidity and RI during the measurements. Polypropylene is used as the main packaging material in packaging of MZI sensor due to its mechanical properties such as low young modulus, relative high tensile stress and breaking strain (Anon., 1999-2001). The sensor was sandwiched in between two polypropylene slabs by mean of cyanoacrylate adhesive, which has a good strain coupling ability over other type of adhesives methods (Clements, 2006). Moreover, the non-covalent adhesive property of the cyanoacrylate only invokes

polymerization at the surface Polypropylene, which will neither destroy the structure of polymer nor cause changes of property to the packaging. Figures 3.4 (a) and (b) show the captured image and schematic diagram of the MZI sensor with a 5.0 cm × 0.5 cm × 0.1 cm Polypropylene packaging.

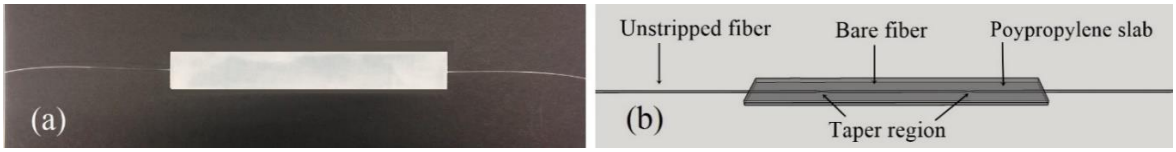

Figure 3.4. The (a) captured image and (b) schematic diagram of MZI Sensor packaged in pristine thickness.

3.3 Fabrication and Packaging of LMZI Sensor

Figure 3.5 shows two tapers with 0.032 mm and 0.030 mm diameters were fabricated on a SMF fiber by using a similar in-house fabrication rig. A fiber loop with 1.5 cm diameter was spooled in between two tapers. Figure 3.6 indicates the captured image of the LMZI sensor which packaged onto a Polyvinyl chloride base by mean of cyanoacrylate adhesive.

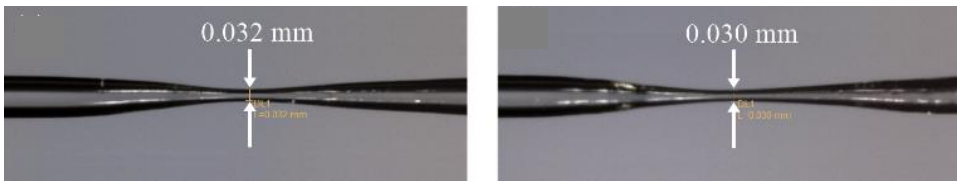

Figure 3.5. Captured image of the first and second taper of the LMZI sensor.

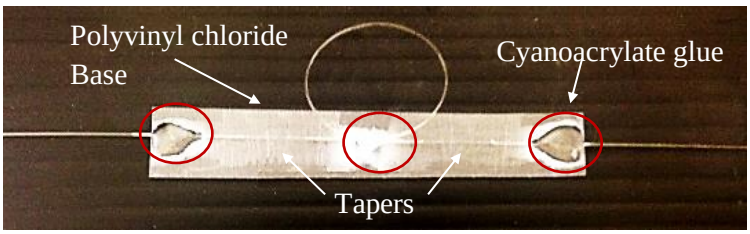

Figure 3.6. Captured image of the LMZI sensor.

A thin Polyvinyl chloride base with 0.3 mm thickness was used in the packaging of LMZI sensor to minimize the absorption of vibration from the surface of contact. Both ends of the LMZI were fixed horizontally onto the Polyvinyl chloride base to prevent inaccuracy measurement caused by the inclination of tapers. Besides, the packaging is helpful in terms of versatility and portability as the sensor can be easily installed and uninstalled to change position along the pipe.

3.4 Curvature Sensing using Taper MZI Sensor

3.4.1 Curvature Characterization of MZI Sensor

The optical power variation of the MZI sensor was characterized based on the curvature changes. As shown in Figure 3.7, the MZI sensor was attached onto an 80 cm × 2.5 cm × 0.47 cm steel bar by mean of cyanoacrylate adhesive. The sensor was connected to a broadband laser source and an optical spectrum analyzer (OSA, brand: Yokogawa) for curvature characterization. The MZI sensor was attached at the midspan of steel bar which is expected to experience maximum deflection when the bar is subjected to bending. As for precaution, the characterization was carried out after 24 hours (cure time) of the adhesion to prevent non-uniform strain effect and low curvature coupling of sensor due to viscosity of cyanoacrylate.

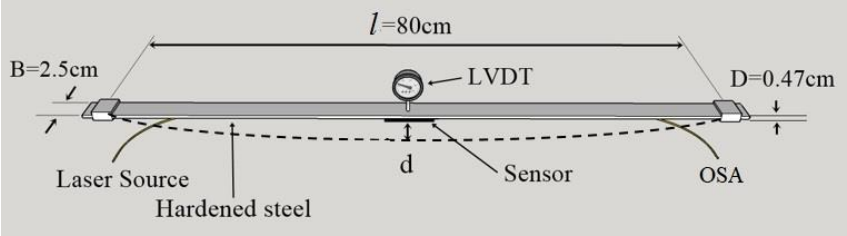

Figure 3.7. The experiment setup of MZI sensor in curvature characterization.

The steel bar was subjected a 2 mm vertical deflection with every 0.25 mm step interval. The resultant power spectrum was recorded using the OSA and the responding curvature, *C* was computed using Equation (5), where *d* is the vertical displacement and *l* is the supporting span.

$$C = \frac{8d}{4d^2 + l^2} \tag{5}$$

3.4.2 Lab Test in Low Weight Foamed Concrete

Three LWFCS beams (reinforcement ratio: 0.942 %; dimension: 115 × 181 × 2300 mm; density: 1700kg/m3) with different percentages of polypropylene fiber (beam 1: 0.4 %; beam 2: 0.25 %; beam 3: 0 %) were prepared for the lab test, to characterize the performance of MZI sensors under different tensile capacities. Polypropylene fiber is a synthetic fiber used in concrete reinforcement which has low density, fine diameter and low modulus of elasticity, high strength, ductility and durability (Alsadey & Salem, 2016). Tensile capacities of beams are related proportionally to the percentages of polypropylene fiber, whereby a higher percentage of polypropylene fiber increases tensile capacity of concrete. (Alsadey & Salem, 2016; Kolli, 2013).

Figures 3.8 (a) and (b) show the installation of sensor onto the rebar, whereas (c) and (d) show the geometry of the LWFCS beam. The MZI sensor was attached onto at the midspan of the bottom rebar by mean of cyanoacrylate adhesive, connected to commercial optical loss test set (OLTS, brand: FiberO), which consists of a laser source and an optical power meter. Operating wavelengths 1550 nm was used in the measurement, which is the standard communication wavelength in the optical communication industry and easily accessed compares to other optical wavelengths. Noted that, the 1550 nm wavelength has a low transmission loss $\leq 0.18 dB/km$ in SMF. As shown in Figure 3.8 (a), a lead wire alloy foil strain gauges (brand: TML, model: FLK-6-11) was attached on the same rebar the opposite side of the MZI sensors for measurement comparison.

Both of the top and bottom surfaces of rebars were grinded superficially to create flat surfaces for MZI sensor and strain gauge, to ensure a strong adhesion. The strong adhesion ensures the that strain experienced by the rebars are coupled to the devices efficiently. The LWFCS beams were casted with concrete and left for 28 days in referring to ASTM C192 (2007) and ASTM C31 (2008) standards. This is to ensure that the beams are fully cured before proceed to the lab test.

Figure 3.9 depicts the installation of LWFCS beams onto the 4-points bending test machine with three Linear Variable Displacement Transducers (LVDTs) installed at the bottom of the beams to record the vertical deflection upon the continuous loading. During the lab test, the loader imposes a loading force of 6 kN to the LWFCS beams upon initialization. The loading force was followed by increment of 1kN per step until the beams failure. Simultaneously,

the resultant optical power and strain were measured by the MZI sensor and strain gauges respectively. The optical power variation was calibrated to the curvature changes experienced by the LWFCS beams for every set of experiment.

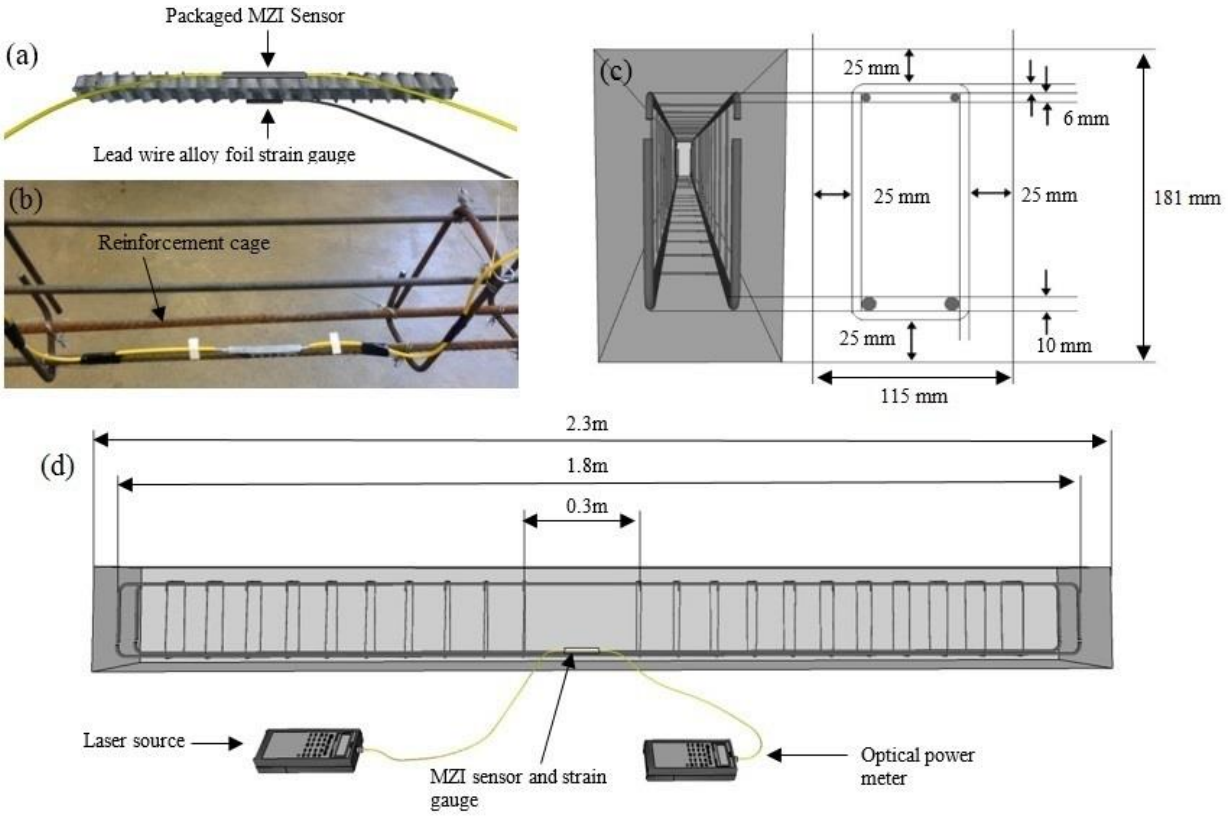

Figure 3.8. (a) and (b) Installation of MZI sensor and strain gauge on the rebar; (c) and (d) geometry of the LWFCS beam.

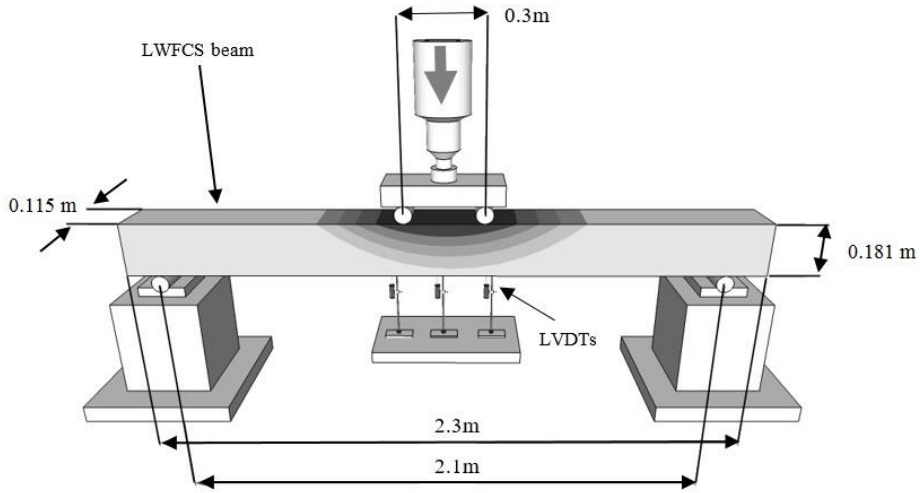

Figure 3.9. Installation of reinforced LWFCS beam on the 4-points bending test machine

3.5 Vibration Sensing using LMZI Sensor

3.5.1 Frequency Characterization of LMZI Sensor

Figure 3.10 shows the experimental set up of the frequency characterization of LMZI sensor. An acoustic source is powered by a 13 A current and controlled by a frequency generator to produce low frequency vibration within 20 Hz to 500 Hz. The sensor is located 2 cm away from the top of the diaphragm, input with a single wavelength (1550 nm) optical laser source (FiberO, FLS-30A) and output to a photodetector (THORLABS, InGaAs Biased detector, DET08CFC/M). The resultant optical signal was converted to electrical signal by photodetector and observed by using an digital oscilloscope (PicoScope; 3203DMSO; Resolution: 1 GS/s; Bandwidth: 50 MHz).

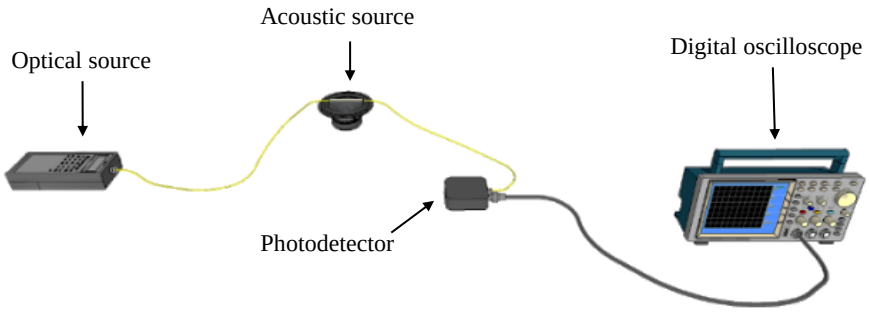

Figure 3.10: Experimental set up of characterization of LMZI sensor in responding to variation of frequency.

3.5.2 Lab Test on Small-scale Pipeline and 40 m Large-scale Pipeline

Figure 3.11 depicts a 3 m galvanized steel pipe (4 cm inner diameter, thickness 1.5-2.5 mm) which was constructed for the preliminary lab test. A 3 mm leak hole was drilled wittingly for purpose of simulating the real condition of leakage. The leak hole was designed so that the screw can be mounted and unmounted to turn on and off the leak. The sensor was attached onto the surface of pipe to ensure that the vibration able to be coupled effectively to the LMZI sensor. To ensure the consistency of measurement, 20 sets of repeatability tests were done for signal averaging.

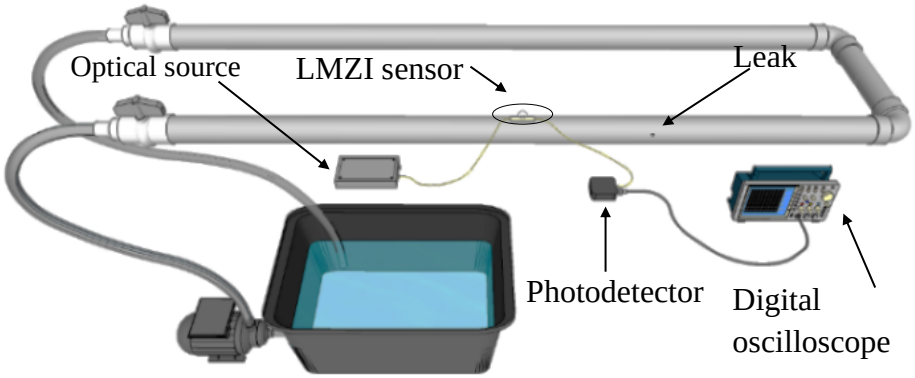

Figure 3.11: Experimental set up of the small-scale pipeline test.

The sensor was then tested on a 40 m large-scale galvanized steel pipeline (8 cm inner diameter, thickness 4-4.4 mm), which was designed with a tunable water pressure up to 3 bar and flow rate 269 gallon/min, as well as controllable leak hole which can be turned on and off to interchange the normal flow and leak condition. Figure 3.12 shows the experimental set-up where the sensor is installed on the 40 m pipeline at 1 m, 2 m, 3 m, and 4 m away from the leak. The measurements were conducted in normal flow and leak condition at both 2 bar and 3 bar water pressure. 20 sets of repeatability tests were done for purpose of data averaging. The measurements were compared to the Accelerometer (model: Kistler 8704B50T) in term of the leak-induced frequencies for verifying purpose.

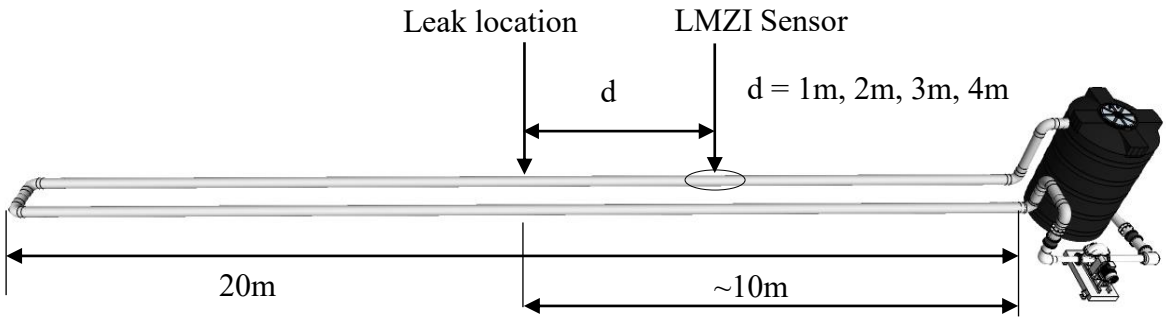

Figure 3.12: Experimental set up of the 40 m large-scale pipeline test.

Figure 3.13: Captured image of the 40 m pipeline test rig.

CHAPTER 4

RESULTS AND DISCUSSIONS

4.1 Curvature Sensing using Taper MZI Sensor

4.1.1 Curvature Characterization of MZI Sensor

Figure 4.1 shows the resultant power spectra taken from the OSA, when the steel bar was subjected to a 2 mm vertical deflection. Shifting in wavelength and power fluctuation was observed across the spectrum. The result is tally with the expectation brought in Equations (2) and (3). To further analyze the characterization in term of power variation, two distinct wavelengths (1550 nm and 1620 nm) were selected from Figure 4.1 to be plotted against the curvature changes in Figure 4.2. The curvature was computed from the vertical deflection by using Equation (5). Figure 4.2 indicates the linear curves at 1550 nm and 1620 nm have an opposite trend (an upward-trend in 1550 nm and a downward-trend in 1620 nm), which are resulted by the different FSR shiftings across the wavelength. Linear curve at 1550 nm has a higher linearity (regression value, R^2=0.9968) compared to 1620 nm (regression value, R^2=0.7404), which is more preferable in the curvature sensing. Linearity is an important criterion in curvature sensing as it is a lot easier if the optical power variation can be related linearly to the curvature. Furthermore, sensitivity of MZI at 1550 nm is better than 1620 nm which is of 1.654 $\mu W/m^{-1}$ at 1550 nm -0.451 $\mu W/m^{-1}$ at 160 nm.

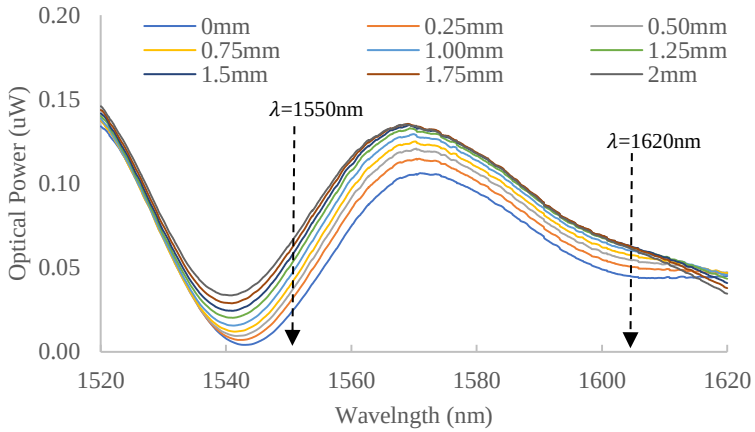

Figure 4.1: Spectral plotting of the MZI sensor imposed to deflection up to 2mm.

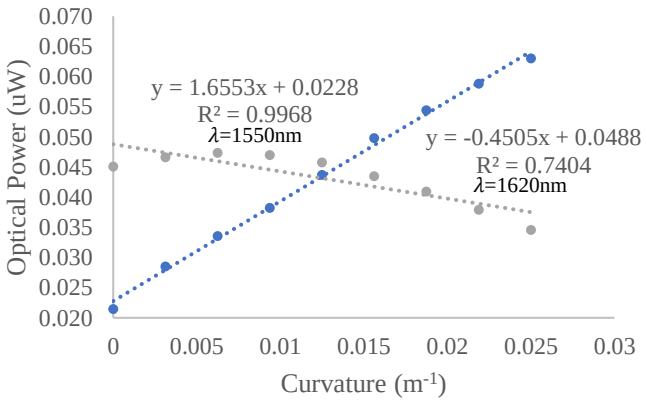

Figure 4.2: Linear curve at 1550 nm and 1620 nm against the curvature changes.

4.1.2 Curvature Detection and Crack Monitoring in Low Weight Foamed Concrete

Figures 4.3, 4.4 and 4.5 show the resultant optical powers of MZI sensor 1, 2 and 3 which were mapped to measurements of the strain gauge 1, 2 and 3, respectively. To elaborate the optical power variation in a clear manner, the data representation was done by sectioning the optical power plot into 3 discrete regions, namely the linear sensing region, internal cracking region and yielding region. Linear sensing region includes the power variation during the elastic

deformation of the rebar, whereby the optical power responds directly to the curvatures of the rebars. As shown in the subsets of Figures 4.3, 4.4 and 4.5, the resultant optical powers of MZI sensors are linearly proportional to the respective curvature changes. The MZI sensors achieved good agreement with the respective strain gauges, with correlation coefficients (MZI sensor 1-strain gauge1: -0.956; MZI sensor 2-strain gauge2: -0.895, and MZI sensor 3-strain gauge3: 0.968).

Internal cracking region comprises the power fluctuation when the curvature of LMFCS beam is high enough to cause internal cracking, thereby fluctuation of optical powers was observed. During internal cracking, shear deformation breaks the concretes into granular fragments. The fragments impose nonuniform movements and forces to the upper surface of MZI sensor, thereby the optical power started to fluctuate accordingly. However, the degree of power fluctuation in MZI sensors are different in three beams. The maximum fluctuation powers were compared in Figure 4.3, 4.4 and 4.5 (MZI sensor 1:0.02 μW; MZI sensor 2: 0.04 μW; MZI sensor 3: 0.28 μW). The degrees of fluctuations were found related to the percentages of polypropylene fiber mixture in the LMFCS beams (beam 1: 0.4 %, beam 2: 0.25 %, beam 3: 0 %). A higher percentage of polypropylene fiber enhances the tensile capacity and cohesiveness of concrete (Alsadey & Salem, 2016) therefore reduces the free moving granular fragments inside the concrete.

The third region which is the yielding region consists of the responding optical power during the yielding of rebar. At this point, elastic deformation ends and continues with the inelastic deformation, the elongation of rebar increases tremendously and causes the failure of beam immediately. However

only MZI sensor 1 managed to detect the yielding, as can be observed in Figure 4.3, the optical power in MZI sensor 1 dropped significantly as the same time as the strain gauge. In beam 2 and beam3, severe internal cracking of LWFCS beams broke the MZI sensors 2 and 3 before the yielding of rebar.

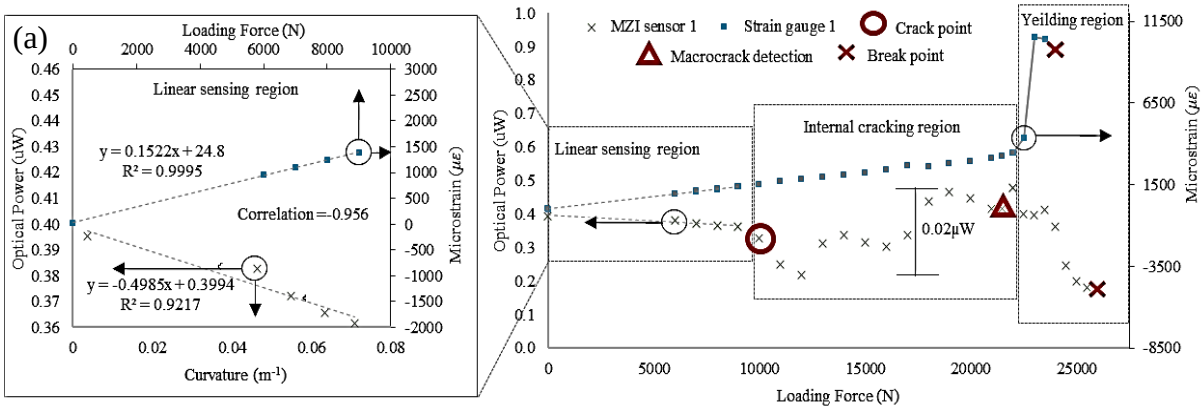

Figure 4.3: Mapping of optical power of sensor 1 to micro-strain of strain gauge 1 in beam 1 (0.4 % polypropylene)

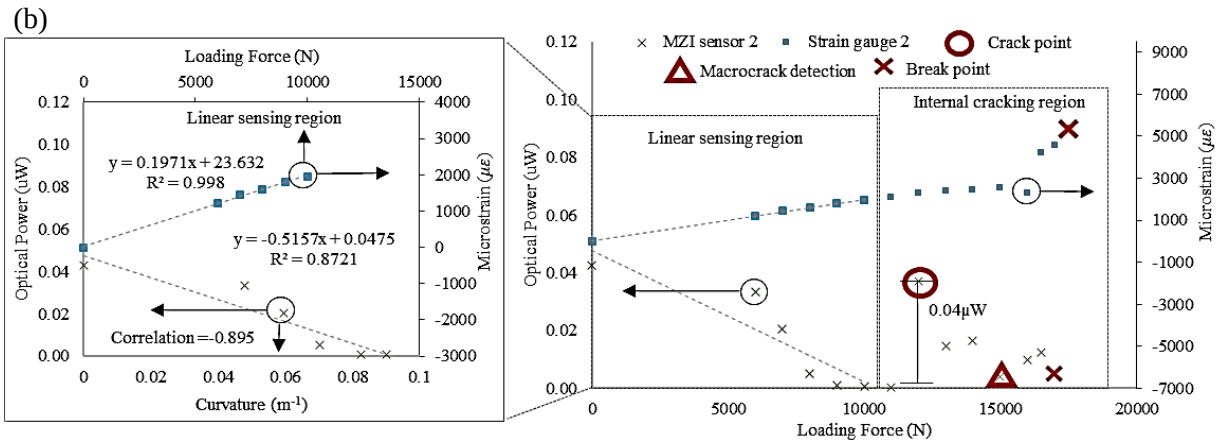

Figure 4.4: Mapping of optical power of sensor 2 to micro-strain of strain gauge 2 in beam 2 (0.25 % polypropylene).

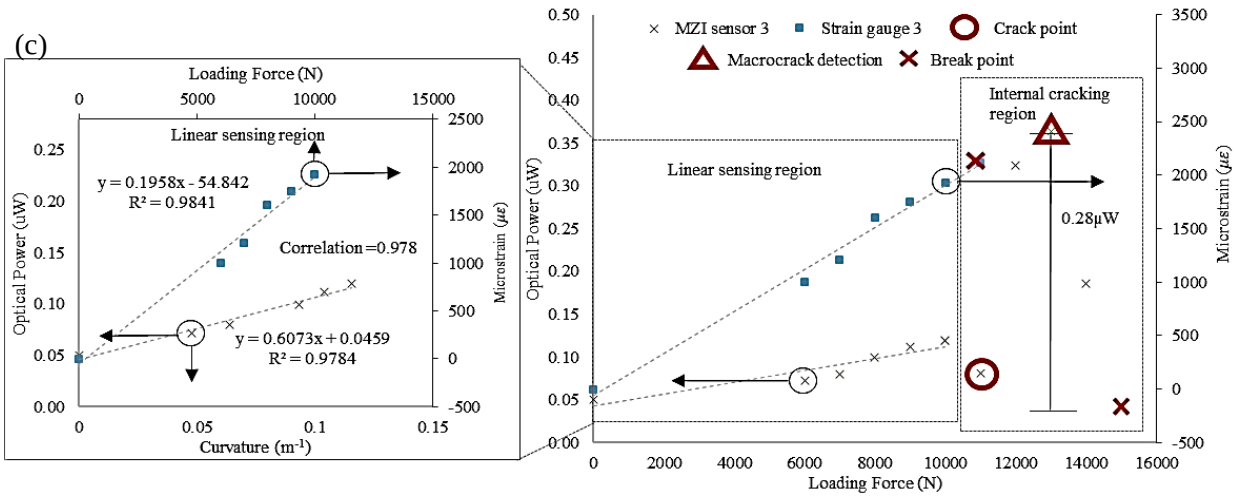

Figure 4.5: Mapping of optical power of sensor 3 to micro-strain of strain gauge 3 in beam 3 (0 % polypropylene).

Figures 4.6, 4.7 and 4.8 depict the surface cracks of beam 1, beam 2 and beam 3 respectively at each successive loading. The labels of 'hairline cracks' and 'macrocracks' differentiate the degree of surface crack. Hairline crack is minor crack which can barely observed by bare eyes and can be recover by implementing epoxy injection for curing (Kunieda, et al., 2001). Macrocrack is the severe crack easily observed on the beam surface which is irrevocable. The macrocracks were spotted on beams 1, 2 and 3 upon loading force of 21.5 kN, 15 kN and 13 kN respectively. By referring to Figures 4.3, 4.4 and 4.5, three of the MZI sensors able to detect the internal cracking before the macrocrack, where the first detections of the internal cracks are marked as the 'crack point'. The early detection of internal cracking before the macrocrack has an advantage over the conventional strain gauge in concrete monitoring. In Figures 4.3, 4.4 and 4.5, the 'break points' mark the failures of the MZI sensors and strain gauges in each beam, which show that the MZI sensors have high sustainability as they managed to survive until the beams completely fractured. A summarization comprises the crack points, macrocrack detections, break points

and sensitivities were tabulated in table 4.1. Table 4.2 shows the correlation coefficients of MZI sensors 1, 2 and 3 mapped to strain gauges 1,2 and 3 respectively. High correlation coefficients between the sensors and strain gauges indicate that the curvatures of LWFCS beams measured by the sensors are close to the strain gauges. The negative correlation coefficients between MZI sensors and strain gauges 1 and 2 are due to the negative power variations of MZI sensors 1 and 2. The real conditions of destruction of the beams 1, 2 and 3 at the end of lab tests are shown in Figures 4.9 (a), (b) and (c).

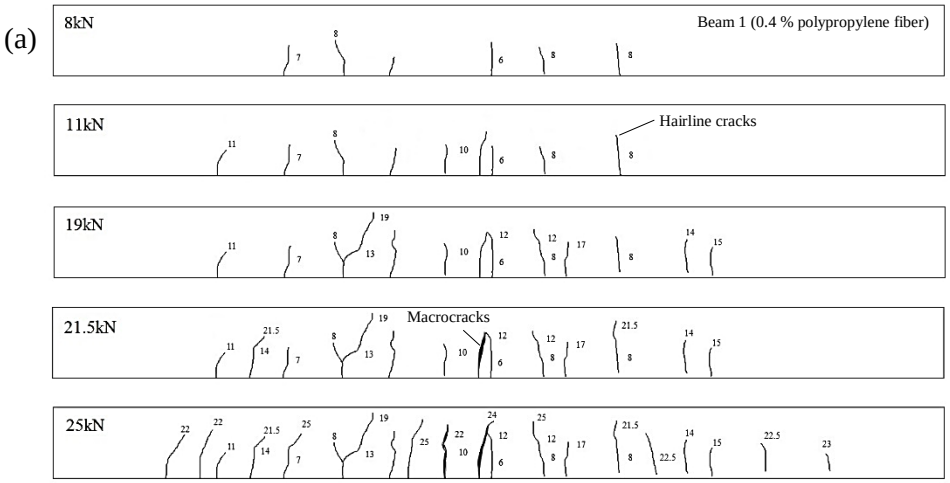

Figure 4.6. Mapping of fracture pattern on beam 1 to the successive strength (represented using red circles in Figure 4.3).

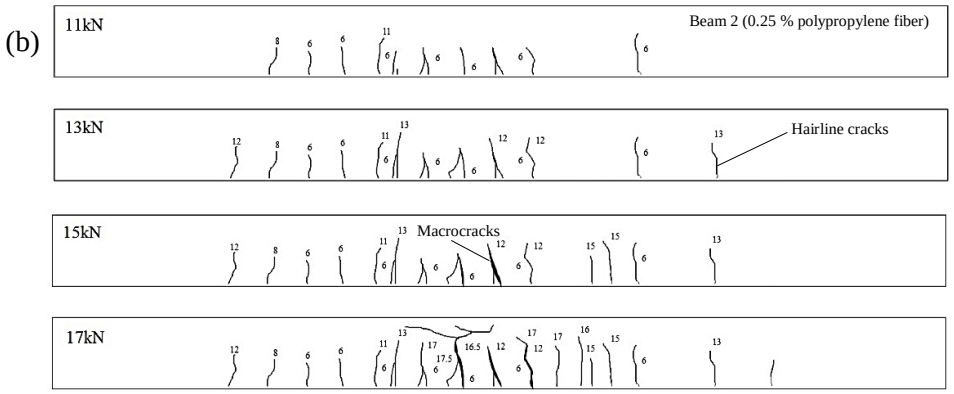

Figure 4.7: Mapping of fracture pattern on beam 2 to the successive strength (represented using red circles in Figure 4.4).

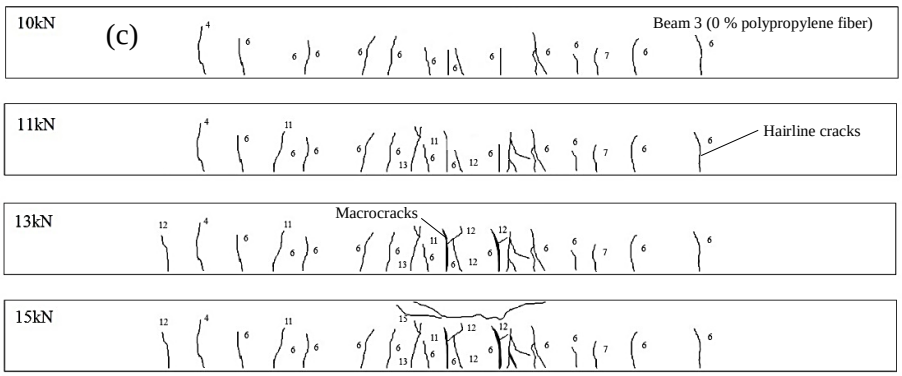

Figure 4.8: Mapping of fracture pattern on beam 3 to the successive strength (represented using red circles in Figure 4.4).

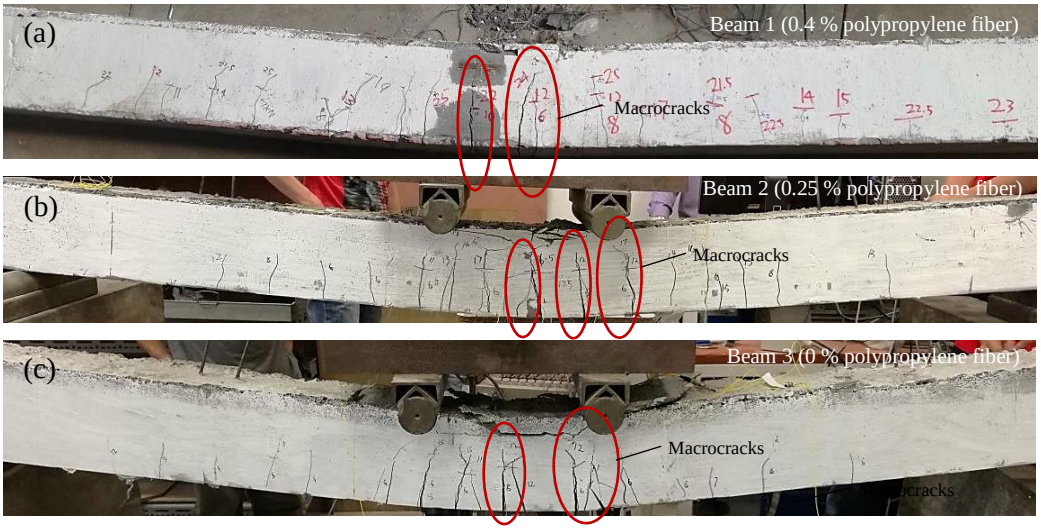

Figure 4.9. (a) Photos of the actual fracture pattern of beam 1; (b) Photos of the actual fracture pattern of beam 2; (c) Photos of the actual fracture pattern of beam 3.

Table 4.1: Summary table of crack point, macrocrack detection, break point and curvature sensitivities for MZI sensor 1, 2 and 3.

	MZI sensor			Strain gauge		
Sensor	1	2	3	1	2	3
Crack point (kN)	10	12	11	NA	NA	NA
Macrocrack detection (kN)	21.5	15	13	NA	NA	NA
Break point (kN)	26	17	15	24	17.5	11
Sensitivity $(\mu W m^{-1})/(\mu\varepsilon N^{-1})$	-0.499	-0.516	0.607	0.152	0.197	0.196

Table 4.2: Correlation coefficients of MZI sensors 1, 2 and 3 mapped to strain gauges 1,2 and 3 respectively

	Correlation coefficient
MZI sensor 1 - Strain gauge 1	-0.956
MZI sensor 2 - Strain gauge 2	-0.895
MZI sensor 3 - Strain gauge 3	0.968

4.2 Vibration Sensing using LMZI Sensor

4.2.1 Torsional Sensitivity of LMZI Sensor

A characterization test was conducted to characterized the optical power variation of LMZI sensor in responding to the torsion. Figure 4.10 shows the result recorded by using OSA which comprises the resultant optical powers when the fiber loop is imposed with a torsion angle up to 35°. A significant power variation was observed in the spectrum, especially at the peak of the wavelength at 1530 nm. A subplot at wavelength 1530 nm was plotted against the torsion angle to study the effect of torsion angle to the optical power. Result indicates that the optical power varies linearly with the torsion and the LMZI sensor able to achieve a torsion sensitivity of 0.0216 μW/°.

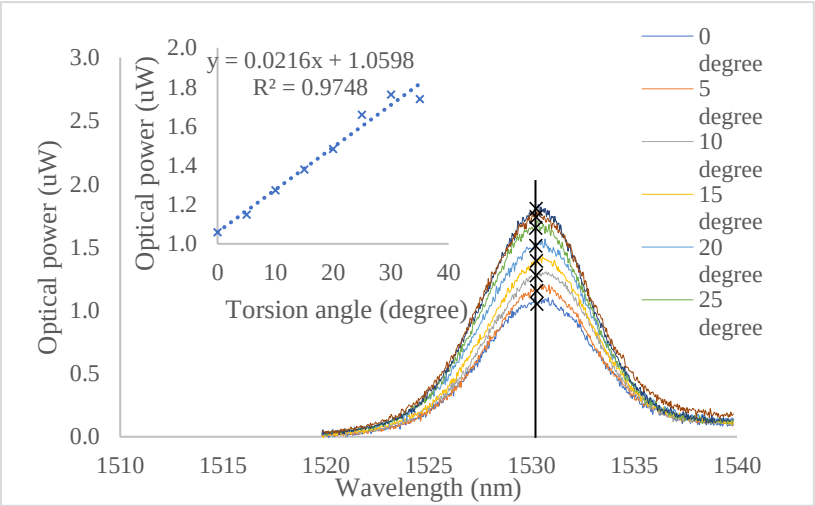

Figure 4.10: Optical power variation in respond to the torsion of LMZI sensor and inset of power variation at wavelength 1530 nm

4.2.2 Frequency Characterization of LMZI Sensor

Frequency characterization was conducted by imposing the low frequency vibration ranges from 20 Hz to 500 Hz to the LMZI sensor. The responding time domain signal was recorded using oscilloscope. By performing the fast Fourier transform (FFT), post filtering and smoothing process, an combination plot of the detected frequency against the source frequency was shown in Figure 4.11. The characterization has confirmed that the LMZI sensor has an accurate frequency response therefore is reliable to be implemented in the vibration sensing.

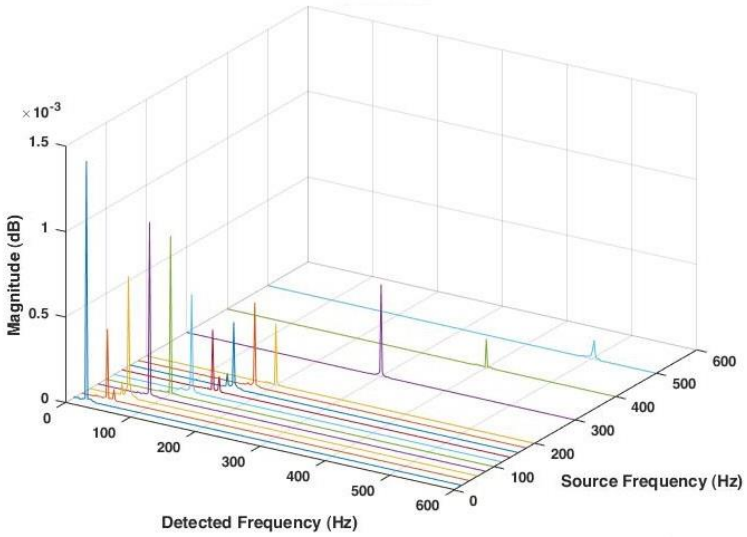

Figure 4.11: Overlapped plot of the frequency characterization in responding to variation of frequency (20 Hz-500 Hz).

4.2.3 Leak Detection in Small-scale Pipeline

Figure 4.12 shows the time domain signals recorded from the oscilloscope when the pipe at rest, in normal flow condition and in leak condition. Distinct differences in term of amplitude can be observed among the three conditions, where the leak condition has the most significant pulses compares to the normal flow condition and pipe at rest. The pulses are caused by the uncontrolled water surge at the leak spot and the air suction, as the bubbling sounds were heard during the leak test.

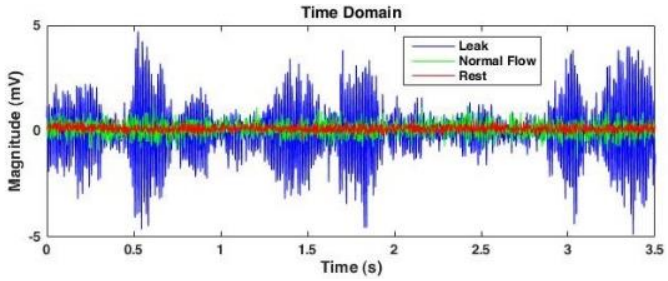

Figure 4.12: Time signal when pipe at rest, in normal flow condition and in leak condition.

Figures 4.13 (a) and (b) show the frequency signals at rest and in normal flow condition, whereby a prominent flow-induced frequency was observed at 37.8 Hz. However, the flow-induced frequency shifts toward 40 Hz during leak, as can be observed in Figure 4.14 (a). Besides, an additional 79.6 Hz frequency appears as during leak. The occurrence of leak-induced frequency was generated as the water collides onto the pipe wall while escaping from the leak hole (Khulief & Khalifa, 2012). Several sets of measurements were done by varying the distances of LMZI sensor at 60 cm, 90 cm and 120 cm away from the leak site to study the effect of leak at various distances. Result shows that the leak-induced frequency damped when the distance of sensor is further away from the leak site, as the 79.6 Hz peak weakened when the LMZI sensor was located at 90 cm and 12 cm from the leak site.

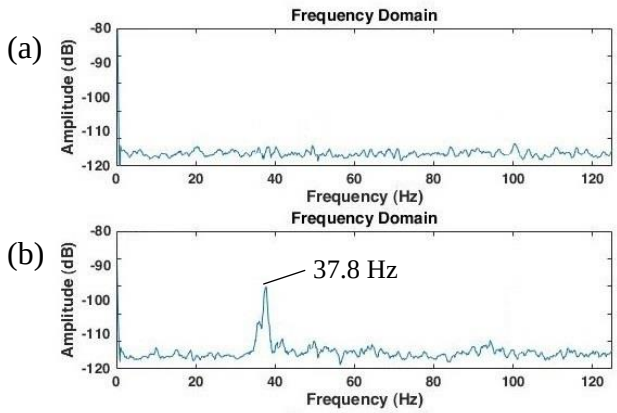

Figure 4.13: Frequency signal when pipe (a) at rest and (b) in normal flow condition.

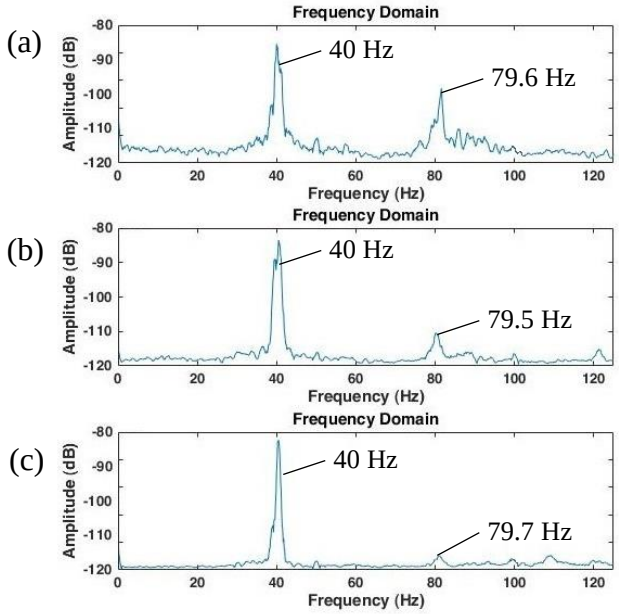

Figure 4.14: Frequency signal when LMZI sensor responded to the leak at (a) 60 cm (b) 90 cm and (c) 120 cm away.

4.2.4 Leak Detection in 40 m large-scale Pipeline

Figure 4.15 (a) shows the resultant signal when the pipe in 2 bar normal flow condition, whereas Figures 4.15 (b), (c), (d) and (e) indicate the responding frequencies in 2 bar leak condition when LMZI sensor was located at distances 1 m, 2 m, 3 m, and 4 m away from the leak. A prominent flow-induced frequency appears at 29.8 Hz during the normal flow condition and shifted to 40.5 Hz when the pipeline was subjected to leak. Besides, an additional 98.4 Hz leak-induced frequency emerged during leakage, which is incurred by the impaction of shockwave on the pipe wall as the water escaped from the leak hole (Thompson, et al., 2001; Khulief & Khalifa, 2012). When the distance of the LMZI sensor is varied across the pipe from the leak site, the amplitude of the leak-induced frequencies at 40.5 Hz and 98.4 Hz dropped as the vibrating source is further away.

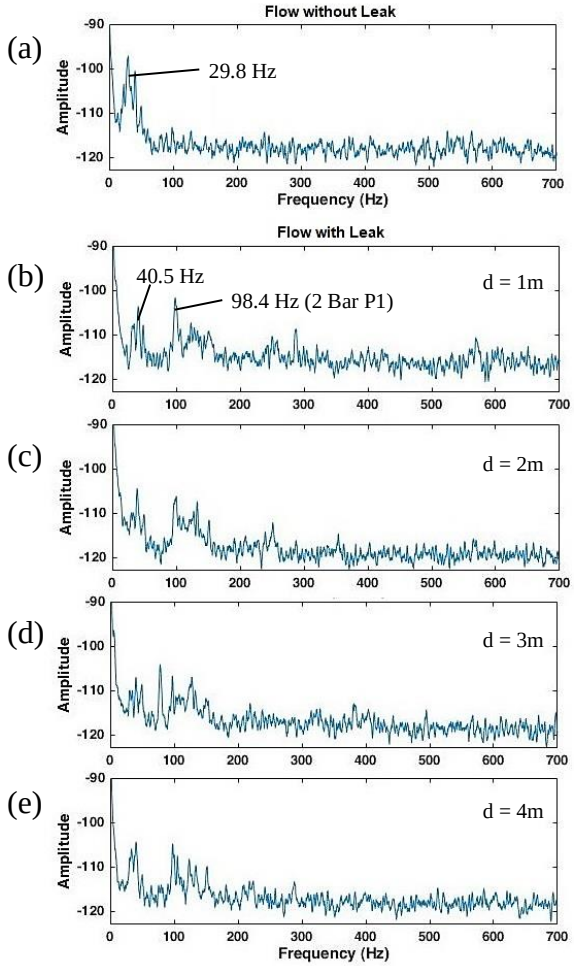

Figure 4.15: Detected frequency when pipe (a) in 2 bar normal flow condition, 2 bar leak condition when the LMZI sensor was located (b) 1 m, (c) 2 m, (d) 3 m, and (d) 4 m away from the leak site.

Figure 4.16 (a) shows the resultant signal when the pipe in 3 bar normal flow condition, whereas Figures 4.16 (b), (c), (d) and (e) indicate the responding frequencies in 3 bar leak condition when LMZI sensor was located at distances 1 m, 2 m, 3 m, and 4 m away from the leak. As shown in Figure 4.16 (a), the 29.9 Hz flow-induced peak maintained during the 3 bar flow. Besides, a new flow-induced frequency emerged at 242.5 Hz. A similar shifting of the flow-induced 29.9 Hz toward 40.2 Hz was observed during the 3 bar leak, as well as the second flow-induced frequency from the initial 242.5 Hz to 250.3 Hz.

Likewise, the 100.3 Hz leak-induced frequency appeared during leak event at 3 bar. However, a new leak-induced frequency at 288.3 Hz was observed during the 3 bar leak condition. Thompson, et al. reported that the higher leak-induced frequency is possibly caused by the cavitation of water within the pipe when the water leaks at high pressure. The first and second leak-induced frequencies drop across the pipeline when the distance is further away from the vibration source at the leak site, which is tally with the scenario found in the 2 bar leak event.

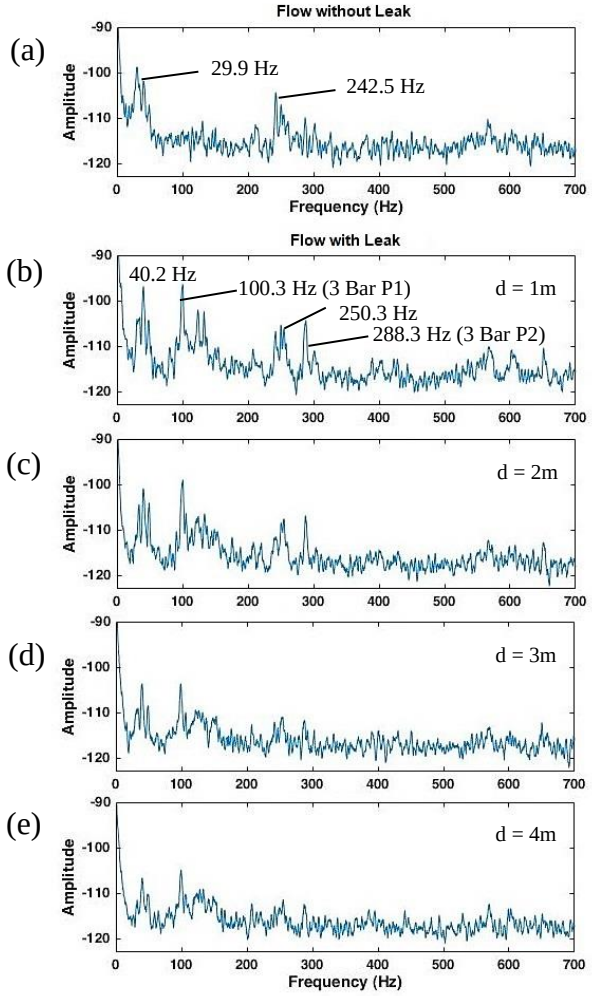

Figure 4.16: Detected frequency when pipe (a) in 3 bar normal flow condition, 2 bar leak condition when the LMZI sensor was located (b) 1 m, (c) 2 m, (d) 3 m, and (d) 4 m away from the leak site.

Figure 4.17 shows the amplitudes of subsequent leak induced-frequencies at 2 bar and 3 bar which were chosen and plotted against the

distance of sensor from the leak site. Where the 2 bar P1 represents the 98.4 Hz peak at 2 bar leak, 3 bar P1 and 3 bar p2 represents the 100.3 Hz and 288.3 Hz peak at 3 bar leak. Result shows that the three leak-induced vibrations on the pipe surface drop linearly across the distance due to damping effect.

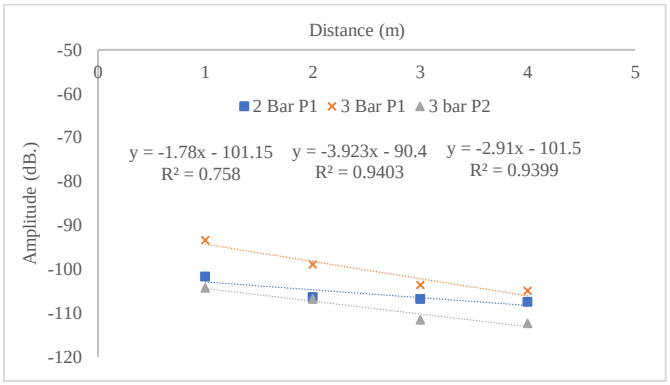

Figure 4.17: The amplitude of subsequent leak induced-frequencies during leak event at 2 bar and 3 bar when the LMZI sensor was located 1 m, 2 m, 3 m, and 4 m away from the leak site.

The leak-induced frequencies in 2 bar and 3 bar leaks were compared to the commercial accelerometer in Figures 4.18 and 4.19, respectively. The frequency responses of both LMZI sensor and accelerometer were compare in the power spectrum density (PSD). The results show good agreement between both measurements, whereby the LMZI sensor and accelerometer able to detect similar leak-induced frequencies (99.5 and 99.1 Hz during leak event at 2 bar, 288.1 Hz and 280.5 Hz during the 3 bar leak event). Percentage variations of the two leak-induced frequencies were calculated, where 0.4% and 2.64% percentage variations were achieved in the 2 bar and 3 bar comparisons, respectively.

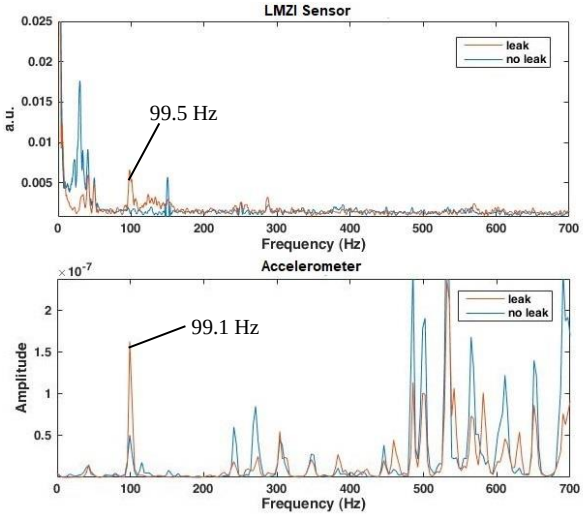

Figure 4.18: PSD signal of LMZI sensor compared to the commercial accelerometer at 2 bar water pressure.

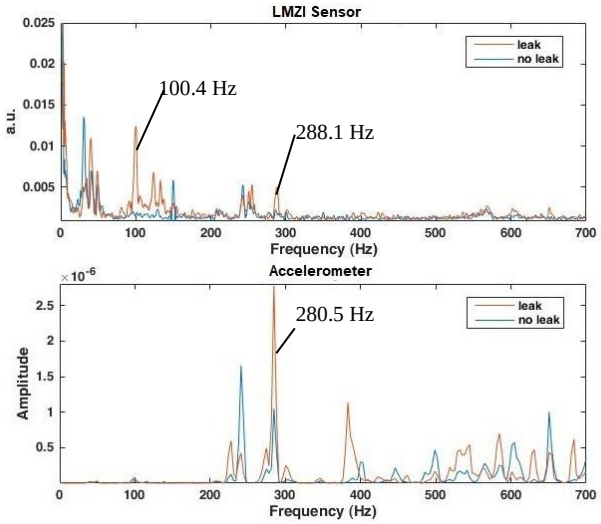

Figure 4.19: PSD signal of LMZI sensor compared to the commercial accelerometer at 3 bar water pressure.

CHAPTER 5

CONCLUSION AND FUTURE WORK

5.1 Conclusion

It was a giant revolution in the sensor development when optical fiber starts to prevail in many sensing applications of structural health monitoring. In this work, a cost-effective in-line tapers MZI sensor with curvature sensitivity up to 1.65 $\mu W/m^{-1}$ was fabricated and characterized according to the LVDT in term of strain. The implementation of MZI sensor into the LWFCS beams was successful as the sensor managed to detect the elongation and yielding of rebar as linearly as the lead wire alloy foil strain gauges (brand: TML, model: FLK-6-11). More importantly, the double-sided sensing property of MZI sensor managed to detect the internal cracking within the concrete before any earlier sighting of the macrocracks, which has advantage over the conventional strain gauge in concrete monitoring.

In the pipeline monitoring, fiber loop segment was integrated in between two tapers to improve the vibrational coupling in MZI sensor. The sensor was designed and characterized at frequency ranges from 20 Hz to 500 Hz to cater for low frequency sensing in leak detection. The LMZI sensor was packaged onto with a Polyvinyl chloride base to provide a simple and portable installing method. In both of the lab-scale and 40 m large-scale pipelines, the LMZI sensor managed to detected different leak-induced frequencies at different water pressures. Moreover, the differences between flow-induced and leak-induced

frequencies are distinct and significant to be differentiate. The frequency responses of the LMZI sensor were compared to the Accelerometer (model: Kistler 8704B50T) and show good agreements, with percentage variations of 0.4% and 2.64% at 2 bar and 3 bar water pressure.

5.2 Recommendations for Future Works

In pipeline monitoring, the feasibilities of LMZI sensor in leak detection was verified. However, in the future work, the sensitivity of sensor can be further improved to cater for the longer distance detection. As a recommendation, improvement in sensitivity can be done by designing a clamp-based packaging to clamp the sensor onto the pipe. Clamping of sensor onto the pipe surface able to improve the vibrational sensitivity as the vibration can be coupled from pipe wall to the sensor more effectively. Besides, modification on term of the sensor's structure such as decreasing the taper diameter can be done to improve the sensitivity of sensor. A smaller taper diameter induces higher attenuation in fundamental mode, as larger portion of fundamental mode splits into the cladding, therefore the sensor is more sensitive to the ambient perturbation.

Furthermore, the distributed sensing system is proposed to be implemented in both concrete monitoring and pipeline monitoring. Distributed sensor able to cater for multiple points sensing therefore provides a better concrete monitoring in large scaled building. In pipeline monitoring, the localization of leak and zone identification can be done by implementing two sensors at different distance along the pipe.

Several multiplexing techniques are suggested as follow for the distributed sensing module. The common found multiplexing technique in MZI sensor is time division multiplexing (TDM). Figure 5.1 illustrates MZI multiplexing technique using TDM in time domain, which comprises a modulator and a 1×N splitter. The modulator is used to manipulates N pulses in vary with time and split them accordingly into the arrays by a splitter. Time delay of each arrays were controlled by the fiber loops with different number of turns.

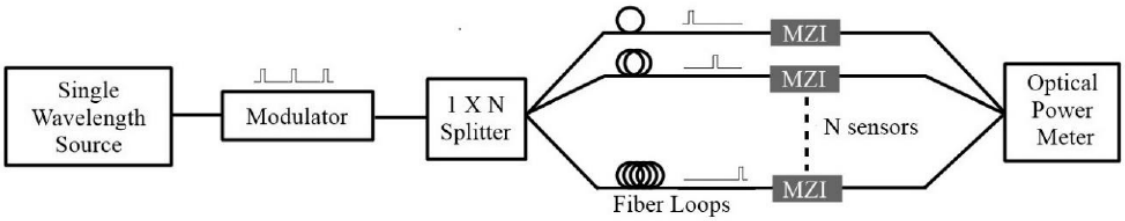

Figure 5.1: Schematic Diagram of MZI Multiplexing Technique using TDM

Figure 5.2 illustrates the MZI multiplexing technique using Subcarrier Multiplexing Method (SMM), which is a costlier and more complicated method. The configuration is slightly different in term of the modulator part, where the modulators are allocated in every array after the splitter, to produce the signals in distinct pulses at various frequencies. The signals with distinct frequency pass though the sensor and respond to the curvature change.

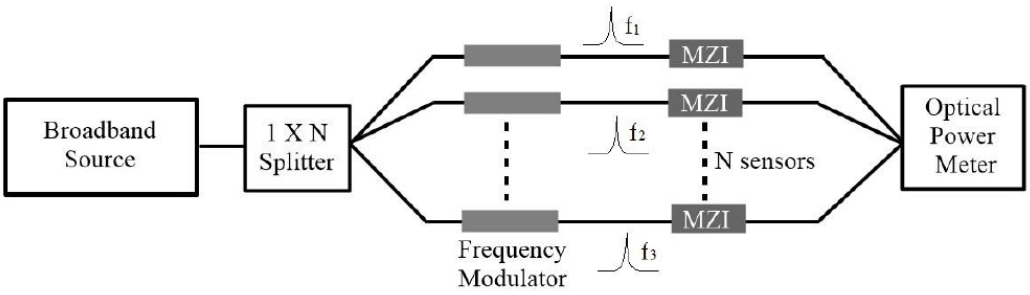

Figure 5.2: Schematic Diagram of MZI Multiplexing Technique using SMM

REFERENCES

Achariam, T., 2016. *Two buried in 6m mud in freak accident* , s.l.: The Sun Daily.

Aggelis, D. G., Soulioti, D. V., Sapouridis, N. & Barkoula, N. M., 2011. Acoustic emission characterization of the fracture process in fibre reinforced concrete. *Construction and Building Materials,* Volume 25, pp. 4126-4131.

Aimé, L. E., Amerigo, T. & Vendramin, G., 2009. *FFT- Based Spectral Response for Smaller Pipeline Leak Detection.* Singapore, IEEE.

Allsop, T., Reeves, R., Webb, D. & Bennion, I., 2002. A high sensitivity refractometer based upon a long period grating Mach-Zehnder interferometer.. *Rev. Sci. Instrum.,* Volume 73, pp. 1702-1705.

Alsadey, S. & Salem, M., 2016. Influence of Polypropylene Fiber on Strength of Concrete. *American Journal of Engineering Research (AJER),* 5(7), pp. 223-226.

Barabanov, S. A. & Glikman, B. F., 2009. The attenuation coefficient of an acoustic wave propagating in a turbulent flow in a long pipeline. *Acoust. Phys.,* 55(2), p. 170–177.

Ben, X., Li, Y., Miao, S. & Zhang, Z., 2012. Acoustic vibration sensor based on nonadiabatic tapered fibers. *Optics Letters,* 37(22), pp. 4768-4770.

Brakel, A. & Swart, P., 2005. Temperature-compensated optical fiber Michelson refractometer. *Opt. Eng.,* Volume 44, pp. 1576-1580.

Charif, A. & Mourad, S. M., 2016. Flexural behavior of beams reinforced with steel bars exceeding the nominal yield strength. *Latin American Journal of Solids and Structures,* 13(5), pp. 945-963.

Chen, D., Liu, W., Jiang, M. & He, S., 2009. High-resolution strain/temperature sensing system based on a high-finesse fiber cavity and time-domain wavelength demodulation.. *J. Lightw. Techol.,* Volume 27, pp. 2477-2481.

Chen, L., Zhang, W. G., Wang, L. & Zhang, H., 2014. In-fiber torsion sensor based on dual polarized Mach-Zehnder interference. *Optics Express,* 22(6).

Chen, X., Yu, Y., Huang, Q. & Wang, J., 2014. Temperature Insensitive Bending Sensor Based On In-Line Mach-Zehnder Interferometer. *Photonics Sensors,* Volume 4(3), pp. 193-197.

Choi, H., Kim, M. & Lee, B., 2007. All-fiber MachZehnder type inferferometric formed in photonics crystal fiber. *Opt. Express,* 15(9), pp. 5711-5720.

Choi, H., Kim, M. & Lee, B., 2007. All-fiber Mach-Zehnder type interferometers formed in photonic crystal fiber. *Opt. Express,* Volume 15, pp. 5711-5720.

Choi, H., Park, K. & Lee, B., 2008. Photonic crystal fiber interferometer composed of a long period fiber grating and one point collapsing of air holes. *Opt. Lett.,* Volume 33, pp. 812-814.

Choi, H., Park, K. & Park, S., 2008. Miniature fiber-optic high temperature sensor based on a hybrid structured Fabry-Perot interferometer. *Opt. Lett.,* Volume 2455-2457, p. 33.

Clohessy, A. M., Healy, N., Murphy, D. F. & Hussey, C. D., 2005. Short low-loss nanowire tapers on singlemode fibres. *Electron. Lett. 41 (17),* p. 954–955.

Dass, S. & Jha, R., 2015. Micron wire assisted Inline Mach-Zehnder Interferometer Curvature Sensor. *Photonics Technology Letters, IEEE* , PP(99).

Deng, M., Tang, C., Zhu, T. & Rao, Y., 2011. PCF-based Fabry-Perot interferometric sensor for strain measurement at high temperatures. *IEEE Photon. Technol. Lett.,* Volume 23, pp. 700-702.

Dermawan, A., 2016. *Indonesian worker dies after under-construction building in Penang collapses,* s.l.: New Straits Times.

Ding, J., Zhang, A. & Shao, L., 2005. Fiber-taper seeded long-period grating pair as a highly sensitive refractive-index sensor. *IEEE Photon. Technol. Lett.,* Volume 17, pp. 1247-1249.

Frazao, O., Aref, S., Baptista, J. & Santos, J., 2009. Fabry-Perot cavity based on a suspended-core fiber for strain and temperature measurement. *IEEE Photon. Technol. Lett.,* Volume 21, pp. 1229-1231.

Frazao, O., Silva, S., Viegas, J. & Baptista, J., 2010. All fiber Mach-Zehnder interferometer based on suspended twin-core fiber. *IEEE Photon. Technol. Lett.,* Volume 22, pp. 1300-1302.

Gao, S., Zhang, W., Bai, Z. & Zhang, H., 2013. Ultrasensitive refractive index sensor on microfiber-assisted U-shape cavity. *Photonics technology Letters,* 25(18), pp. 1815-1818.

Gong, Y., Zhoa, T., Rao, Y. & Wu, Y., 2011. All-Fiber Curvature Sensor Based On Multimode Interference. *Photonics Technology Letter, IEEE,* 23(11), pp. 679-681.

Harris, A. J. & Castle, P. F., 1986. Bend Loss Measurements on High Numerical Aperture Single-Mode Fibers as a Function of Wavelength and Bend Radius. *Journal of Lightwave Technology,* LT-4(1), pp. 34-401.

Harun, S. W., Lim, K., Jasim, A. & Ahmad, H., 2010. Fabrication of tapered fiber based ring resonator. *Laser Physics,* 20(7), p. 1629–1631.

Hosford, W. F., 2010. *Mechanical behavior of materials.* s.l.:Cambridge University Press.

Hunaidi, O., 1998. Ground-penetrating radar for detection of leaks in buried plastic water distribution pipes. *Seventh Int. Conf. on Ground-Penetrating Radar,* p. 783–786.

Hunaidi, O., Wang, A., Bracken, M. & Gambino, T., 2004. *Acoustic methods for locating leaks in municipal water pipe networks.* Dead Sea, Jordan, s.n.

Jong, C. S., Won, G. K. & Han, Y. G., 2016. Temperature-Insensitive Microfiber Mach–Zehnder Interferometer for Absolute Strain Measurement. *Journal of Lightwave Technology,* 34(19), pp. 4579-4583.

Karkulali, P. & Mishra, H., 2016. *Leak Detection in Gas Distribution Pipelines using Acoustic Impact Monitoring.* Florence, Italy, IEEE, pp. 23-26.

Khulief, Y. A. & Khalifa, E. A., 2012. *On the In-Pipe Measurements of Acoustic Signature of Leaks in Water Pipelines.* s.l., Reseach Gate.

Kim, D., Zhang, Y., Cooper, K. & Wang, A., 2005. In-fiber reflection mode interferometer based on a long-period grating for external refractive-index measurement. *Appl. Opt.,* Volume 44, pp. 5368-5373.

Kim, M., Kim, Y. & Lee, B., 2008. Simultaneous measurement of temperature and strain based on double cladding fiber interferometer assisted by fiber grating pair. *IEEE Photon. Technol. Lett.,* Volume 20, pp. 1290-1292.

Kim, Y., Kim, M., Park, M. & Jang, J., 2008. Hydrogen sensor based on a palladium-coated long-period fiber grating pair. *J. Opt. Soc. Korea,* Volume 12, pp. 221-225..

Kim, Y., Paek, U. & Lee, B., 2002. Measurement of refractive-index variation with temperature by use of long-period fiber gratings. *Opt. Lett.,* Volume 27, pp. 1297-1299.

Koh, K., 2015. *Three killed, six injured when building floor collapsed,* s.l.: New Straits Times.

Kolli, R., 2013. Strength Properties Of Polypropylene Fiber Reinforced Concrete. *International Journal of Innovative Research in Science,Engineering and Technology,* 2(8).

Kunieda, M., Kamada, T. & kugo, K., 2001. *Flexural failure behavior of concrete beams repaired by crack injection,* Swets & Zeitlinger, Lisse: de Bors.

Kwak, H. G. & Kim, S. P., 2002. Nonlinear analysis of RC beams based on moment–curvature relation. *Computers and Structures ,* Volume 80, p. 615–628.

Lee, M. & Lee, J., 2000. Acoustic emissions technique for pipeline leak detection. *Key Eng. Mater.,* p. 183–187.

Liao, C. R., Wang, D. N. & Wang, Y., 2013. Microfiber in-line Mach–Zehnder interferometer for strain sensing. *Optics Letters*, 38(5), pp. 757-759.

Li, B., Jian, L. & Wang, S. M., 2011. Ultra-Abrupt Tapered Fiber Mach-Zehnder Interferometer Sensors. *Sensors*, Volume 11, pp. 5729-5739.

Lim, J., Jang, H., Lee, K. & Kim, J., 2004. Mach-Zehnder interferometer formed in a photonic crystal fiber based on a pair of long-period fiber gratings. *Opt. Lett.*, Volume 29, pp. 346-348.

Lim, J., Priya, S. S. & & Menon, P., 2016. *DBKL and councils have a system in place to monitor construction sites but all safety aspects come under DOSH*, s.l.: The Star .

Lin, H., Raji, Y., Lim, J. & Lim, S., 2016. Packaged in-line Mach–Zehnder interferometer for highly sensitive curvature and flexural strain sensing. *Sensors and Actuators A: Physical*, Volume 250, p. 237–242.

Lin, H. et al., n.d. Packaged in-line Mach-Zehnder interferometer for highly sensitive curvature and strain sensing. *Journal of Selected Topics in Quantum Electronics.*

Liu, Y., Li, Y., Yan, X. & Li, W., 2015. Effect of waist diameter and twist on tapered asymmetrical dual-core fiber MZI filter. *Applied Optics*, 54(28), pp. 8248-53.

Liu, Y. & Wei, L., 2007. Low-cost high-sensitivity strain and temperature sensing using graded-index multimode fibers. *Physics and Computer Science Faculty Publications.*

Li, W. J., Kong, Q. Z., Ho, S. C. & Lim, I., 2016. Feasibility study of using smart aggregates as embedded acoustic emission sensors for health monitoring of concrete structures. *Smart Materials and Structures*, 25(11).

Lu, P. & Chen, Q., 2010. Asymmetrical fiber mach-zehnder interferometer for simultaneous measurement of axial strain and temperature. *IEEE Photonics Journal*, 2(6), pp. 945-953.

Lu, P., Men, L., Sooley, K. & Chen, Q., 2009. Tapered fiber Mach-Zehnder interferometer for simultaneous measurement of refractive index and temperature. *Appl. Phys. Lett.*, Volume 94.

Machavaram, V., Badcock, R. & Fernando, G., 2007. Fabrication of intrinsic fibre Fabry-Perot sensors in silica fiPero using hydrofluoric acid etching.. *Sen. Actuat.*, Volume 138, pp. 248-260..

Mao, L. L., Sun, Q. Z., Lu, P. & Lao, Z. F., 2015. Fiber up-taper assisted Mach-Zehnder interferometer for high sensitive temperature sensing. *frontiers of Optoelectronics*, 8(4), pp. 431-438.

Meyers, M. & Chawla, K., 2008. *Mechanical Behavior of Materials.* 2nd ed. Melbourne: Cambridge University Press.

Mohd, H., 2016. *Construction worker buried alive in Taman Segambut landslip tragedy.*, s.l.: New Straits Times .

Mokhtar, M. R., Owens, K., Kwasny, J. & Taylor, S. E., 2012. Fiber-Optic Strain Sensor System With Temperature Compensation For Arch Bridge Condition Monitoring. *IEEE SENSORS JOURNAL, VOL. 12, NO. 5*, pp. 1479-1486.

Mokhtar, M. R., Sun, T. & Grattan, K. T. V., 2011. Arch-bridge Lift Process Monitoring by Using Packaged Optical Fibre Strain Sensors with Temperature Compensation. *Journal of Physics: Conference Series*, p. 307.

Mokhtar, M. R., Sun, T. & Grattan, K. T. V., 2012. Bragg Grating Packages With Nonuniform Dimension for Strain and Temperature Sensing. *IEEE SENSORS JOURNAL, VOL. 12, NO. 1*, pp. 139-145.

Morales, A. M. & Lieber, C. M., 1998. A laser ablation method for the synthesis of crystalline semiconductor nanowires. *Science 279 (January (5348))*, p. 208–211.

Morris, P., Hurrell, A., Shaw, A. & Zhang, E., 2009. A Fabry-Perot fiber-optic ultrasonic hydrophone for the simultaneous measurement of temperature and acoustic pressure. *J. Acoust. Soc. Am.*, Volume 125, pp. 3611-3622.

Mudhana, G., Park, K. & Lee, B., 2011. Dispersion measurement of liquids with a fiber optic probe based on a bi-functional lensed photonic crystal fiber. *Opt. Commun.*, Volume 284, pp. 2854-2858.

Mudhana, G., Park, K., Ryu, S. & Lee, B., 2011. Fiber-optic probe based on a bifunctional lensed photonic crystal fiber for refractive index measurements of liquids.. *IEEE Sens. J.*, Volume 11, pp. 1178-1183.

National Water Services Commission, N., 2017. *Non Revenue Water (NRW) 2015-2016.* [Online]
Available at: http://www.span.gov.my/index.php/en/statistic/water-statistic/non-revenue-water-nrw-2017
[Accessed 5th February 2018].

Ngyuen, L., Hwang, D., Moon, S. & Moon, D., 2008. High temperature fiber sensor with high sensitivity based on core diameter mismatch. *Opt. Express*, Volume 16, pp. 11369-11375.

Ni, W. J., Lu, P., Liu, D. M. & Zhang, J. S., 2017. *A highly sensitive twist sensor without temperature cross sensitivity based on tapered single-thin-single fiber offset structure.* s.l., 25th International Conference on Optical Fiber Sensors.

Ong, K. S., Png, W. H., Lin, H. S. & Pua, C. H., 2017. *Acoustic Vibration Sensor Based on Macro-Bend Coated Fiber For Pipeline Leakage Detection.* Jeju, Korea, 17th International Conference on Control, Automation and Systems.

Ong, K. S., Png, W. H., Lin, H. S. & Pua, C. H., 2017. *Detection, Acoustic Vibration Sensor Based on Macro-Bend Coated Fiber For Pipeline Leakage.* Jeju, Korea, 17th International Conference on Control, Automation and Systems.

Park, K., Choi, H., Park, S. & Paek, U., 2010. Temperature robust refractive index sensor based on a photonic crystal fiber interferometer. *IEEE Sens. J.*, Volume 10, pp. 1147-1148.

Pedrotti, F., Pedrotti, L. & Pedrotti, L., 2007. *Introduction to Optics.* Upper Saddle River, NJ, USA,: earson International.

Raijtar, J. M., Muthieh, R. & Scott, L. R., 1994. Pipeline leak detection system for oil spills prevention. In: *Technical Completion Rep., USDOE and NM Waste-Management Education and Research Consortium.* Las Cruces, NM: s.n., p. 601–614.

Raji, Y. M., Lin, H., Ibrahim, S. & Mokhtor, M., 2016. Intensity-modulated abrupt tapered fiber Mach-Zehnder interferometer for simultaneous sensing of temperature and curvature. *Optics & Laser Technology,* Volume 86, pp. 8-13.

Raji, Y. M., Lin, H. S., Ibrahim, S. A. & Mokhtar, E. R., 2016. Intensity-modulated Abrupt Tapered Fiber Mach-Zehnder Interferometer For The Simultaneous Sensing of Temperature and Curvature. *Opticas and Laser Technology,* Volume 86, pp. 8-13.

Ran, J., Rao, Y., Zhang, J. & Liu, Z., 2009. Miniature fiber-optic refractive-index sensor based on laser-machined Fabry-Perot interferometer tip. *J. Lightw. Techol.*, Volume 27, pp. 5426-5429.

Ran, Z., Rao, Y., Liu, W. & Liao, X., 2008. Laser-micromachined Fabry-Perot optical fiber tip sensor for high-resolution temperature-independent measurement of refractive index.. *Opt. Express,* pp. 2252-2263.

Rao, Y., Deng, M., Duan, D. & Yang, X., 2007. Micro Fabry-Perot interferometers in silica fibers machined by femtosecond laser. *Opt. Express,* Volume 15, pp. 14123-14128.

Rocha, M. S., 1989. Acoustic monitoring of pipeline leaks. *SA,* 89(0333).

Shen, C., Zhong, C., You, Y. & Chu, J., 2012. Polarization-Dependent Curvature Sensor Based On In-Fiber Mach-Zehnder Interferometer With A Different Arithmetic Demodulation Method. *Optics Express*, 20(14), pp. 15406-15417.

Shiotani, T., Kunieda, M. & Okude, N., 2010. Quantified estimation of rebar corrosion by means of acoustic emission technique. *Fracture Mechanics of Concrete and Concrete Structures ,* pp. 1149-1153.

Shun, W., Ping, L., Liang, Z. & Liu, D., 2014. Optical fiber acoustic sensor based on nonstandard fused coupler and aluminium foil. *IEEE Sensors Journal,* 14(7), pp. 2293-2298.

Sirkis, J., Brennan, D., Putman, M. & Berkoff, T., 1973. In-line fiber etalon for strain measurement. *Opt. Lett.,* Volume 18, pp. 1973-1975.

Soltanian, M. R. K., Sharbirin, A. S., Ariannejad, M. M. & Amiri, I. S., 2016. Variable Waist-Diameter Mach–Zehnder Tapered-Fiber Interferometer as Humidity and Temperature Sensor. *IEEE Sensors Journal,* Volume 16, pp. 5987-5992.

Sun, H., Yang, S., Zhang, J. & Rong, Q. Z., 2012. Temperature and refractive index sensing characteristics of an MZI-based multimode fiber–dispersion compensation fiber–multimode fiber structure. *Optical Fiber technology,* 18(6), pp. 425-429.

Taghreed, K. M. A., 2014. Flexural behavior of reinforced beams reinforced with corrosive rebar. *International journal of civil and structural engineering ,* 5(1), pp. 64-73.

Thompson, M., Chapman, C. J., Howison, S. D. & Ockendon, J. R., 2001. *Noise generation by water pipe leaks.* Keele University, Staffordshire, England.: 40th European Study Group with Industry.

Tian, Z., Yam, S., Barnes, J. & Bock, W., 2008. Refractive index sensing with Mach-Zehnder interferometer based on concatenating two single-mode fiber tapers. *IEEE Photon. Technol. Lett.,* Volume 20, pp. 8626-628.

Tian, Z., Yam, S. & Loock, H., 2008. Single-mode fiber refractive index sensor based on core-offset attenuation. *Photonics technology Letters,* 20(16), pp. 1387-1389.

Tian, Z., Yam, S. & Loock, H., 2008. Single-mode fiber refractive index sensor based on core-offset attenuators. *IEEE Photon. Technol. Lett,* Volume 16, pp. 1387-1389.

Tsai, W. & Lin, C., 2001. A novel structure for the intrinsic Fabry-Perot fiber-optic temperature sensor. *J. Lightw. Techol.,* Volume 19, pp. 682-686.

Wang, X. Z., 2012. Characterization of Fiber Tapers for Fiber Devices and Sensors. *Ottawa-Carleton Institute for Physics, University of Ottawa.*

Wang, Z., Shen, F., Song, L. & Wang, X., 2007. Multiplexed fiber Fabry-Pérot interferometer sensors based on ultrashort Bragg gratings. *IEEE Photon. Technol. Lett.,* Volume 19, pp. 622-624.

Wan, X. & Taylor, H., 2002. Intrinsic fiber Fabry-Perot temperature sensor with fiber Bragg grating mirrors. *Opt. Lett.,* Volume 27, pp. 1388-1390.

Xing, X., Wang, Y. & Li, B., 2008. Nanofibers drawing and nanodevices assembly in poly(trimethylene terephthalate). *Opt. Express 16 (14),* p. 10815–10822.

Yang, J., Jiang, L., Wang, S. & Li, B., 2011. High sensitivity of taper-based Mach–Zehnder interferometer embedded in a thinned optical fiber for refractive index sensing. *Applied Optics,* 50(28), pp. 5503-5508.

Yin, S. Z., Ruffin, P. B. & Francis, T. S. Y., 2008. *Fiber Optic Sensors Second Edition.* Boca Raton, Florida: CRC Press.

Yuan, L., Yang, J. & Liu, Z., 2008. A compact fiber-optic flow velocity sensor based on a twin-core fiber Michelson interferometer. *IEEE Sens. J.,* Volume 8, pp. 1114-1117.

Zendehnam, A., Mirzaei, M., Farashiani, A. & Farahani, L. H., 2010. Investigation of bending loss in a single-mode. *PRAMANA - Journal of Physics,* 74(4), p. 91{603.

Zhang, Y., Chen, X., Wang, Y. & Cooper, K., 2007. Microgap multicavity Fabry-Pérot biosensor. *J. Lightw. Techol.,* Volume 25, pp. 1797-1804.

Zhao, J., Huang, X., He, W. & Chen, J., 2010. High-resolution and temperature-insensitive fiber optic refractive index sensor based on fresnel reflection modulated by Fabry-Perot interference.. *J. Lightw. Techol.,* Volume 28, pp. 2799-2803.

Zhou, Q., Zhang, W. G. C. L. & Yan, T. Y., 2015. Fiber torsion sensor based on a twist taper in polarization-maintaining fiber. *Optics Express,* 23(18), pp. 23877-23886.

Zhu, J., Zhang, A., Xia, T. & He, S., 2010. Fiber-optic high-temperature sensor based on thin-core fiber modal interferometer. *IEEE Sens. J.,* Volume 10, pp. 1415-1418.

LIST OF PUBLICATIONS

Png, W. H., Lin, H. S., Pua, C. H., Lim, J. H., Lim, S. K., Lee, Y. L. & Rahman, R. A., 2018. Feasibility use of in-line Mach–Zehnder interferometer optical fibre sensor in lightweight foamed concrete structural beam on curvature sensing and crack monitoring. *Structural Health Monitoring*. Volume 17(5), pp. 1277–1288.

Png, W. H., Lin, H. S., Pua, C. H., & Rahman, R. A., 2018. Pipeline monitoring and leak detection using Loop integrated Mach Zehnder Interferometer optical fiber sensor. *Optical Fiber Technology*. Volume 46, pp. 221-225.